

**Numerical investigation on the effect of transversal fluid field deformation on heat transfer in a rod bundle with mixing vanes**

Tas-Köhler, S.; Lecrivain, G.; Krepper, E.; Unger, S.; Hampel, U.;

Originally published:

February 2020

**Nuclear Engineering and Design 361(2020), 110575**

DOI: <https://doi.org/10.1016/j.nucengdes.2020.110575>

Perma-Link to Publication Repository of HZDR:

<https://www.hzdr.de/publications/Publ-30737>

Release of the secondary publication  
on the basis of the German Copyright Law § 38 Section 4.

CC BY-NC-ND

# Numerical investigation on the effect of transversal fluid field deformation on heat transfer in a rod bundle with mixing vanes

Sibel Tas-Koehler <sup>a,b,\*</sup>, Gregory Lecrivain <sup>a</sup>, Eckhard Krepper <sup>a</sup>, Sebastian Unger <sup>a</sup>,  
Uwe Hampel <sup>a,c</sup>

<sup>a</sup> Helmholtz-Zentrum Dresden-Rossendorf, Institute of Fluid Dynamics, Bautzner Landstr. 400, 01328 Dresden, Germany

<sup>b</sup> Middle East Technical University, Department of Mechanical Engineering, Dumlupınar Blv. No: 1, 06800 Ankara, Turkey

<sup>c</sup> Technische Universität Dresden, Chair of Imaging Techniques in Energy and Process Engineering, 01062 Dresden, Germany

\* CORRESPONDING AUTHOR (E-MAIL: [s.tas@hzdr.de](mailto:s.tas@hzdr.de))

## ABSTRACT

Spacer grids of fuel rod assemblies are equipped with vanes, which promote flow mixing and turbulence within and across the sub-channels, thereby enhancing the heat transfer. First, a literature study about the various effect of the spacer grid has on the sub-channel thermo-hydrodynamics is provided. It follows, that the multiple effects on the vane angle are insufficiently understood. The effect of the vane angle on design parameters, namely the evolution of the Nusselt number, the pressure drop, the cross and swirl flows, is here further discussed and supplemented by own simulations. The effect of the velocity gradient tensor  $\nabla \otimes \mathbf{u}$ , decomposed into a strain and a vorticity contribution, is also looked at downstream of the spacer grid. The RNG k- $\epsilon$  turbulence model was found to provide results best matching the experimental data available in the literature. The use of vanes results in the formation of a downstream vortex. As the flow develops downstream of the spacer grid, the vortex migrates away from the sub-channel center and eventually weakens. In line with the presented literature survey, it is confirmed that a vane angle of about 30° provides optimal swirl and cross flows, resulting in an enhanced heat transfer.

Keywords: Literature analysis, Vortex generator, Vane angle, Rod bundle, Vorticity, Turbulent flow, Heat transfer.

## Nomenclature

### Latin symbols

$c_p$	specific heat [ $\text{J kg}^{-1} \text{K}^{-1}$ ]
$D$	rod diameter [m]
$D_h$	hydraulic diameter [m]
$g$	coordinate in G direction [m]
$G$	minimum distance between the rod surfaces [m]
$L$	axial length [m]
$L_e$	entrance length [m]
$l_{\text{spacer}}$	spacer grid length [mm]
$h$	heat transfer coefficient [ $\text{W m}^{-2} \text{K}^{-1}$ ]
$k$	turbulent kinetic energy [ $\text{m}^2 \text{s}^{-2}$ ]
$Nu$	Nusselt number [-]
$Re$	Reynolds number [-]
$P$	rod pitch [m], pressure [Pa], turbulent energy production [ $\text{kg m}^{-1} \text{s}^{-3}$ ]
$r$	radial distance from the centre of the sub-channel [m]
$R$	effective swirl radius [m]
$S_{ij}$	rate-of-strain tensor [ $\text{s}^{-1}$ ]
$q$	wall heat flux [ $\text{W m}^{-2}$ ]
$T, T_b, T_w$	temperature, bulk temperature, wall temperature [K]
$U$	mean flow velocity [ $\text{m s}^{-1}$ ]
$U_a$	local axial velocity [ $\text{m s}^{-1}$ ]
$U_b$	axial velocity averaged over a cross-sectional plane [ $\text{m s}^{-1}$ ]
$U_{\text{lat}}$	lateral velocity [ $\text{m s}^{-1}$ ]
$U_{\text{tan}}$	tangential mean velocity [ $\text{m s}^{-1}$ ]
$u'$	time-averaged fluctuating velocity [ $\text{m s}^{-1}$ ]
$u, v, w$	velocity in x, y, z [ $\text{m s}^{-1}$ ]
$W$	vane base length [m]
$t$	time [s]

### Greek symbols

$\lambda$	thermal conductivity [ $\text{W m}^{-1} \text{K}^{-1}$ ]
$\rho$	density [ $\text{kg m}^{-3}$ ]
$\varepsilon$	turbulence dissipation rate [ $\text{m}^2 \text{s}^{-3}$ ]
$\mu$	dynamic viscosity [ $\text{kg m}^{-1} \text{s}^{-1}$ ]
$\mu_t$	turbulent viscosity [ $\text{kg m}^{-1} \text{s}^{-1}$ ]
$\Phi$	viscous dissipation function [ $\text{s}^{-2}$ ]
$\omega$	vorticity [ $\text{s}^{-1}$ ], turbulence frequency [ $\text{s}^{-1}$ ]
$\Omega_{ij}$	rate-of-rotation tensor [ $\text{s}^{-1}$ ]
$\tau_{ij}$	stress tensor [ $\text{kg m}^{-1} \text{s}^{-2}$ ]
$\delta_{ij}$	Kronecker delta function
$\alpha$	vane angle [ $^\circ$ ]

30

### 31 Acronyms

32 CFD: computational fluid dynamics

33 CHF: critical heat flux

34 LDA: Laser Doppler anemometry

35 LDV: Laser Doppler velocimetry

36 LSVF: large scale vortex flow

37 RMS: root mean square

38 RNG: re-normalization group

39 RSM: Reynolds stress model

40 SAS: scale-adaptive simulation

41 SSG: Speziale-Sarkar-Gatski

42 SST: shear stress transport

43 TKE: turbulent kinetic energy

44 TVSG: twist vane spacer grid

## 45 1. Introduction

46 In a nuclear reactor, the fission heat must be efficiently removed from the surface of the fuel rods by the  
47 coolant fluid. In the event of critical heat flux (CHF), the formation of a local film boiling with low heat  
48 transfer may potentially lead to cladding damages. A preventing measure to counteract this risk is to  
49 support the fuel rods with spacer grids equipped with vanes generating swirl and cross flows. These  
50 vanes (or vortex generators) promote both the near-wall turbulence and the enthalpy exchange between  
51 the sub-channels. Measuring the local flow and the heat transfer is, however, experimentally difficult.  
52 Thus, there has been a continuous interest in employing Computational Fluid Dynamics (CFD)  
53 simulations. The following section provides a brief, yet detailed, state-of-the-art summary on the recent  
54 numerical and experimental studies in the field.

55 Hereafter, the Reynolds number ( $Re$ ) is defined with the mean velocity inlet ( $U$ ), the hydrodynamic  
56 diameter of the sub-channel cross-section ( $D_h$ ), and the kinematic viscosity of the coolant fluid ( $\eta$ ). The  
57 hydrodynamic diameter ( $D_h$ ) is defined with the rod diameter ( $D$ ) and the rod pitch ( $P$ ). The Nusselt  
58 number ( $Nu$ ) is defined with the thermal conductivity of the rod material ( $\lambda$ ) and the heat transfer  
59 coefficient ( $h$ ). This latter ( $h$ ) is defined with the applied heat flux ( $q$ ), the bulk temperature ( $T_b$ ), and  
60 the wall temperature ( $T_w$ ). The Reynolds number, the hydraulic diameter, the Nusselt number, and the  
61 heat transfer coefficient are given by

$$Re = \frac{U D_h}{\eta}, \quad (1)$$

$$D_h = D \left[ \frac{4}{\pi} \left( \frac{P}{D} \right)^2 - 1 \right], \quad (2)$$

$$Nu = \frac{h D_h}{\lambda}, \quad (3)$$

$$h = \frac{q}{T_b - T_w}. \quad (4)$$

62 Besides, the swirl flow factor ( $S_r$ ) and the cross-flow factor ( $C_r$ ) are defined as

$$S_r = \frac{1}{R} \int \frac{U_{\tan}}{U_a} dr, \quad (5)$$

$$C_r = \frac{1}{G} \int \frac{|U_{\text{lat}}|}{U_b} dg, \quad (6)$$

63 with the tangential mean flow velocity component ( $U_{\tan}$ ), the local axial component ( $U_a$ ), the radial  
64 distance from the centre of the sub-channel ( $r$ ), the effective swirl radius ( $R$ ), the lateral velocity  
65 component ( $U_{\text{lat}}$ ) perpendicular to the axial direction ( $g$ ), the axial velocity averaged over a cross-  
66 sectional plane ( $U_b$ ), and the minimum distance between the rod surfaces ( $G$ ). The length ( $L$ ) is also  
67 defined as the axial distance from the vane tips.

### 68 1.1 Flow hydrodynamics downstream of the spacer grid

69 The flow hydrodynamics have been studied for various types of vanes and vane angles. Table 1 and  
70 Table 2 present a list of recent experimental and numerical works respectively dealing with the flow  
71 dynamics downstream of a spacer grid.

72

Researchers	Laboratory condition	Type of spacer grid	Aim of the study
Chang <i>et al.</i> (2008) [1]	Laser Doppler Anemometry (LDA) 5x5 rod bundle $Re = 50,000$	Split vane (30°) Swirl vane (35°)	Analysis of turbulent flow mixing in a rod bundle
Chang <i>et al.</i> (2014) [2]	LDA 5x5 rod bundle $Re = 48,000$	Split vane Swirl vane	Investigation of turbulent flow structures
Wang <i>et al.</i> (2016) [3]	Laser induced fluorescence (LIF) 3x3 rod bundle $Re = 2010$	Split type	Analysis of and visualization of the fluid mixing process in a rod bundle
Shen <i>et al.</i> (1991) [4]	LDV 4x4 rod bundle $Re = 14,200$	Mixing blades (0°, 20°, 25°, 30°, 35°)	Distributions of transverse mean velocity and RMS velocity
Holloway <i>et al.</i> (2008) [5]	Temperature measurements 5x5 rod bundle $Re = 29,000 - 35,000$	Standard grid Split vane (30°) Disc vane	Investigation of convection-induced heat transfer
Byun <i>et al.</i> (2018) [6]	LDV 6x6 rod bundle $Re = 30,000 - 50,000$	Split type Large scale vortex flow type (30°)	Heat transfer characteristics for downstream flow in the support grid
In <i>et al.</i> (2015) [7]	Temperature measurements 3x3 rod bundle $Re = 42,000$	Twisted vane (35°)	Investigation of the convective heat transfer enhancement in a rod bundle by twist-vane spacer grid.
Moon <i>et al.</i> (2014) [8]	Temperature measurements 6x6 rod bundle $Re = 1121 - 13,600$	Split vane	Heat transfer enhancement by spacer grids in single-phase steam flow
Han <i>et al.</i> (2009) [9]	LDA 6x6 rod bundle $Re = 50,000$	Tandem arrangement vanes (30°)	Investigation the thermal hydraulic flow characteristics in sub-channels
Caraghiaur <i>et al.</i> (2009) [10]	LDV 24 fuel rod bundle $Re = 10,000 - 50,000$	Standard grid	Investigation of the phenomena that govern turbulent flows in fuel rod assemblies with spacers
Ikeda (2014) [11]	Laser Doppler velocimetry (LDV) 5x5 rod bundle $Re = 40,000 - 50,000$	Split vane (30°)	Investigation the local velocity profile in a rod bundle and inside a spacer grid.
McClusky <i>et al.</i> (2003) [12]	Particle image velocimetry (PIV) 5x5 rod bundle $Re = 28,000$	Split vane (30°)	Investigation of lateral flow
Xiong <i>et al.</i> (2014) [13]	LDV 6x6 rod bundle $Re = 6600 - 70,300$	Standard grid	Investigation of the turbulent flow
Qu <i>et al.</i> (2019) [14]	PIV 5x5 rod bundle $Re = 39,600$	Mixing vane	Systematically optimization of PIV for lateral flow measurements / analysis of systematic and random errors

74 **Table 1:** Summary of experimental studies on flow in rod bundles taken from the literature.

75 Bhattacherjee *et al.* [15] showed, that a square spacer grid with two mixing vanes has as much influence  
76 on the flow hydrodynamics as a circular spacer grid equipped with two symmetric mixing vanes. Chang  
77 *et al.* [1] found, that a split vane generates higher turbulence intensity and anisotropy than a swirl type  
78 vane. Kim *et al.* [16] showed, that split vanes, which produce flow separation because of the adverse  
79 pressure gradient near the rod surfaces, prevent cross-flow. Cui *et al.* [17] showed, that the swirl factor  
80 peaks at position  $L \approx 4 D_h$  for various vane types, namely for vanes with a 35° twist angle, vanes with  
81 a 45° twist, and split vanes. Wu *et al.* [18] found, that a 45° vane angle generates more persistent flow  
82 vortices in planes normal to the streamwise direction. Chang *et al.* [2] found, that a split vane provides  
83 a better mixing efficiency between the sub-channels than a swirl vane. They concluded, that a 25° vane  
84 angle is best and, that a 35° vane angle is unfavourable. Cheng *et al.* [19] showed, that the mixing  
85 coefficient, defined as the ratio of lateral velocity to mean entrance velocity, increases with both the  
86 vane angle and the length of the split vane. Wang *et al.* [3] found, that the mixing rapidly decreases from  
87 the vane tip  $L = 0$  to  $L \approx 4 D_h$ . In the work of In [20], split-vanes and twisted-vanes were found to  
88 provide a higher mixing rate for both swirl and cross-flow than side-supported vanes and swirl vanes.  
89 Shen *et al.* [4] showed, that a higher vane angle generally results in a higher mixing and a more  
90 heterogeneous mixing rate.

91 In the presence of spacer grid, the flow velocity is strongly anisotropic due to high swirling flow  
92 dynamics, flow separation, and sudden changes in the strain rate. Hence, the choice of a suitable  
93 turbulence model is crucial to achieving an accurate flow prediction. Numerous studies focusing on the

94 turbulence modelling of the flow in rod bundles can be found in the literature (See Table 2 for a recent  
 95 summary).

Researchers	Turbulence model	Simulation condition	Spacer grid type	Aim of the study
Kim <i>et al.</i> (2005) [16]	Standard k- $\epsilon$	Two sub-channel Wall function	Split vane (25°) Split vane with cut-out (29°)	Optimization of shape of the mixing vanes/understanding flow characteristics and heat transfer
Bhattacharjee <i>et al.</i> (2017) [15]	Large eddy simulations (LES)	flow around a rod $Re = 8900$ $y^+ = 3$	Square spacer grid Circular spacer grid Mixing vane (30°)	Effect of mixing vane on flow hydrodynamics
Cui <i>et al.</i> (2003) [17]	Standard k- $\epsilon$	Single sub-channel $Re = 80,000$	NJ type vane (25°) Split vane (25°)	Effect of different vane shapes on flow structure and heat transfer
Wu <i>et al.</i> (2017) [18]	Standard k- $\epsilon$ , SST k- $\omega$ , RSM	Four sub-channel $Re = 40,000 - 120,000$ Wall function	Rectangular longitudinal vortex generators (30°,45°, 60°)	Thermal-hydraulic characteristics of the sub-channel/effect of vane angle
Cheng <i>et al.</i> (2017) [19]	SST k- $\omega$	5x5 rod bundle	Split vane (25°, 31°, 37°,43°)	Influence of vane angle and vane length
In (2001) [20]	Standard k- $\epsilon$	Single sub-channel $Re = 65,000$ $y^+ = 15$	Split vane (30°) Side-supported vane Swirl vane Twisted vane (35°)	Impact of the vane angle on the induced swirl flow structure and the turbulent kinetic energy
Díaz <i>et al.</i> (2015) [21]	Standard k- $\epsilon$ , RNG k- $\epsilon$ Realizable k- $\epsilon$ , Standard k- $\omega$ , SST k- $\omega$	flow around a pipe $Re = 40,000$ Wall function	Swirl disturbance generators	Comparison of the different Reynolds-Averaged Navier-Stokes (RANS) models
Gandhir <i>et al.</i> (2011) [22]	Realizable k- $\epsilon$ , SST k- $\omega$	5 x 5 rod bundle $Re = 23,000$	Split vane	Examination of the effect of the selection of an appropriate turbulence model
Hosokawa <i>et al.</i> (2012) [23]	Standard k- $\epsilon$ , Launder-Sharma k- $\epsilon$ model	2x2 rod bundle $Re = 25,000$ $y^+ = 4-30$	Standard grid	Measurements of 3D velocity and turbulence intensities/ comparison with the simulations
Xiong <i>et al.</i> (2014) [24]	SSG RSM, baseline RSM	3x3 rod bundle $Re = 15,200$ Wall function	Standard grid	Validation against experimental results
Holloway <i>et al.</i> (2006) [25]	Realizable k- $\epsilon$ , SST k- $\omega$ , RSM	Two sub-channel $Re = 35,000$ $y^+ \sim 1$	Split vane (30°)	Investigation of the swirl flow and vortex effects downstream of the vanes
Conner <i>et al.</i> (2010) [26]	RNG k- $\epsilon$	5 x 5 rod bundle $y^+ = 40-100$	Split vane	Effect of computational mesh, turbulence model and the boundary conditions with comparison to benchmark experiments
Cinosi <i>et al.</i> (2014) [27]	Standard k- $\epsilon$ , Standard k- $\omega$ , RSM	5 x 5 rod bundle $Re = 50,000$ $y^+ = 0.05-7$	Split vane (30°)	Improvement of the modelling with validation of MATiS-H (Measurements & Analysis of Turbulence in Subchannels – Horizontal) tests
Podila <i>et al.</i> (2016) [28]	Realizable k- $\epsilon$ , SST k- $\omega$ , RSM	5 x 5 rod bundle $Re = 50,000$ $y^+ = 0.04-40$	Split vane	Prediction of the turbulence intensities and velocity variation downstream of the split-vane spacer grid
Chen <i>et al.</i> (2017) [29]	Standard k- $\epsilon$ , Realizable k- $\epsilon$ , RNG k- $\epsilon$ , RSM, SST k- $\omega$	Four sub-channel $y^+ = 30-60$	Split vane	Hybrid application of multiple Reynolds Averaged Navier-Stokes (RANS) models for the computational efficiency
Chen <i>et al.</i> (2017) [30]	RNG k- $\epsilon$ , SST k- $\omega$ , Standard k- $\epsilon$ , BSL RSM	5x5 rod bundle $Re = 14,600 - 34,800$ $y^+ = 30$	Split vane	Selection of an appropriate turbulence model
Chen <i>et al.</i> (2016) [31]	Standard k- $\epsilon$ , Realizable k- $\epsilon$ , RNG k- $\epsilon$	5 x 5 rod bundle $Re = 20,000$ $y^+ = 31-42$	Split vane Hybrid vane	Investigation on thermal-hydraulic behaviour downstream of the spacer grid
Xiong <i>et al.</i> (2018) [32]	Standard k- $\epsilon$ Realizable k- $\epsilon$	4 x 4 rod bundle $y^+ = 1$	Twisted vane (35°)	Accuracy of Standard and Realizable k- $\epsilon$ model in predicting the swirling flow/ decay of swirling flow/evolution of turbulence
Koncar <i>et al.</i> (2018) [33]	SST- Scale adaptive simulation (SAS)	5 x 5 rod bundle $Re = 50,000$ $y^+ = 0.2-10$	Split vane	Comparison of MATiS-H test results with flow simulations
Li <i>et al.</i> (2014) [34]	SST k- $\omega$	5x5 rod bundle Wall function	Split vane (25°)	Computational effort of numerical methods for 17x17 large bundles
Chen <i>et al.</i> (2016) [35]	Standard k- $\epsilon$ , Realizable k- $\epsilon$ , RNG k- $\epsilon$ , SST k- $\omega$ , RSM	4x4 rod bundle 2x2 rod bundle	Split vane Swirl vane	Effect of simplified boundaries and region size
Liu <i>et al.</i> (2012) [36]	SST k- $\omega$ , Realizable k- $\epsilon$ , RNG k- $\epsilon$ , Standard k- $\omega$ , RSM	5x5 rod bundle Four sub-channel $Re = 28,000 - 42,000$ $y^+ < 1$	Standard grid Split vane (30°)	Effect of boundary conditions, turbulence model, mesh refinement and turbulence near-wall treatment
Tseng <i>et al.</i> (2014) [37]	SST k- $\omega$	Two sub-channel $Re = 35,000$	Split vane (30°)	Investigation of the thermal-hydraulic characteristics in a rod bundle with split-vane pair grids
Liu <i>et al.</i> (2010) [38]	RSM	Four sub-channel $Re = 28,000$ $y^+ = 31-48$	Standard grid Split vane (30°)	Investigation of the effects of different types of grid on the turbulent mixing and heat transfer enhancement
Lifante <i>et al.</i> (2014) [39]	SST k- $\omega$ , BSL RSM	3x3 rod bundle $y^+ \sim 4$	Standard grid	Analysis of secondary flow
Agbodemegbe <i>et al.</i> (2016) [40]	Non-linear standard k- $\epsilon$ , SST k- $\omega$ , Realizable k- $\epsilon$	5x5 rod bundle $Re = 34,000$ $y^+ = 11-31$	Split vane (30°)	Investigation of predictability of CFD/analysis of effect of split vane on cross-flow

Ikeda <i>et al.</i> (2006) [41]	Standard k- $\epsilon$ ,	5x5 rod bundle $y^+ = 30-100$	Split vane	Calculation of pressure loss in strap and mixing vane structures/ investigation of CFD applicability for predicting the CHF
Navarro <i>et al.</i> (2011) [42]	Standard k- $\epsilon$	5 x 5 rod bundle Wall function	Split vane (25°)	Performance of CFD models by comparison with the experimental data taken from the literature
Sohag <i>et al.</i> (2017) [43]	Standard k- $\epsilon$ , Realizable k- $\epsilon$ , Standard k- $\omega$ , SST k- $\omega$ , RSM	1/8 <sup>th</sup> of a sub-channel $Re = 1640 - 12,000$ $y^+ \sim 1$	Standard grid	Investigation of spacer grid blockage ratio and grid spacing with different Re and P/D ratio
Mao <i>et al.</i> (2017) [44]	SST k- $\omega$	5x5 rod bundle	Split vane	Investigation of mixing vane cross-flow in sub-channel
Lee <i>et al.</i> (2014) [45]	Standard k- $\epsilon$ , SST k- $\omega$ , RSM, SST- SAS, Direct /Large Eddy simulations	5 x 5 rod bundle $Re = 50,000$	Split vane	Validation of CFD codes based on the MATiS-H test by synthesizing different numerical studies.
In <i>et al.</i> (2008) [46]	Standard k- $\epsilon$ , RNG k- $\epsilon$	Four sub-channel $Re = 28,000 - 42,000$ $Re = 500,000$ Wall function	Split vane (30°) Hybrid vane	Understanding the heat transfer enhancement/ comparison of the thermal-hydraulic performance for two different mixing vane spacers

96

**Table 2:** Summary of the numerical studies on rod bundle taken from the literature.

97 Díaz *et al.* [21] found, that in the swirl area downstream of the spacer grid, the Standard k- $\epsilon$  turbulence  
98 model is able to simulate the turbulent flow more accurately than the k- $\omega$  model. Gandhir *et al.* [22]  
99 found, that the Shear Stress Transport (SST) k- $\omega$  model provides more accurate results than its  
100 Realizable k- $\epsilon$  counterpart in terms of pressure drop. Hosokawa *et al.* [23] found, that the k- $\epsilon$  model  
101 yields good predictions for the axial velocity distribution in the sub-channel. Xiong *et al.* [24] found,  
102 that the Speziale-Sarkar-Gatski (SSG) model and the baseline Reynolds Stress Model (bRSM) result in  
103 higher axial velocities in the interior and edges of the sub-channel than in the experiments. Holloway *et*  
104 *al.* [25] showed, that the SST turbulence model delivers better results than the Realizable k- $\epsilon$  and RSM  
105 in terms of turbulence intensities. Conner *et al.* [26] showed that the Re-Normalization Group (RNG)  
106 k- $\epsilon$  model delivers results matching best the experimental data. Cinosi *et al.* [27] found, that the k- $\epsilon$ , k-  
107  $\omega$ , and the Reynolds Stress Turbulence (RST) models underestimate the time-averaged fluctuating  
108 velocity components  $u'$ . Podila *et al.* [28] simulated the flow in a rod bundle with the Realizable k- $\epsilon$ , the  
109 SST k- $\omega$  and the RSM models and found, that all turbulence models under-predict the measured  
110 turbulence intensity downstream of the split-vanes. In terms of flow anisotropy in the sub-channel, Chen  
111 *et al.* [29] obtained similar results with both the RSM and the RNG k- $\epsilon$  models. Chen *et al.* [30] found  
112 that, at high Reynolds number ( $Re = 34,800$ ), the SST and the bRSM models deliver results better than  
113 the k- $\epsilon$  model in terms of axial velocity. They also found, that at lower Reynolds number ( $Re = 14,600$ ),  
114 results are better with the k- $\epsilon$  and the RNG k- $\epsilon$  models. Chen *et al.* [31] also tested various turbulence  
115 models and found, that the RNG k- $\epsilon$  model predicts the rotational flow in the sub-channels most  
116 accurately. Simulations by Xiong *et al.* [32] indicated, that both the Realizable k- $\epsilon$  model with curvature  
117 correction and the Standard k- $\epsilon$  model with cubic-closure correction over-predict the decay of the  
118 swirling flow with the length ( $L$ ). Koncar *et al.* [33] compared the Scale-Adaptive Simulation (SAS)  
119 model with an Unsteady Reynolds-averaged Navier-Stokes (URANS)-SST simulation and found, that  
120 it achieves a better agreement than the steady SST k- $\omega$  model in terms of velocity.

## 121 1.2 Heat transfer downstream of the spacer grid

122 Heat transfer enhancement by spacer grids and vanes was also analyzed by several researchers.  
123 Simulations by Liu *et al.* [36] showed good predictions of the Nusselt number at  $Re = 28,000$ . Tseng  
124 *et al.* [37] found an anisotropic heat transfer distribution on the rod surfaces in the azimuthal direction.  
125 Holloway *et al.* [5] reported, that in the presence of split-type vanes, the heat transfer coefficient first  
126 increases in the region  $0 < L < 1.5D_h$  and then decreases exponentially with the streamwise distance  $L$ .  
127 Byun *et al.* [6] also showed, that for the split vane, the heat transfer enhancement occurs in the  
128 region  $0 < L < 10D_h$ . With the exception of the split vane design, Liu *et al.* [38] found, that CFD is  
129 able to predict reasonably well the downstream evolution of Nusselt number  $Nu(L)$ . In *et al.* [7]  
130 experimentally found, that the heat transfer coefficient downstream of the twist vane ( $L > 0$ ) is up by

131 about 30% compared to the region upstream of the vanes ( $L < 0$ ). Moon *et al.* [8] showed, that heat  
 132 transfer enhancement is only observable beyond  $Re > 10,000$ . Vane angle and vane type have also been  
 133 found to significantly influence the heat transfer enhancement. Wu *et al.* [18] showed, that a  $45^\circ$  vane  
 134 angle provides the largest heat transfer rate along the sub-channel. Findings of Kim *et al.* [16] showed,  
 135 that the split vanes, cause the occurrence of temperature peaks at the rod surfaces.

### 136 1.3 Conclusion to the above current state of the art and motivations of this work

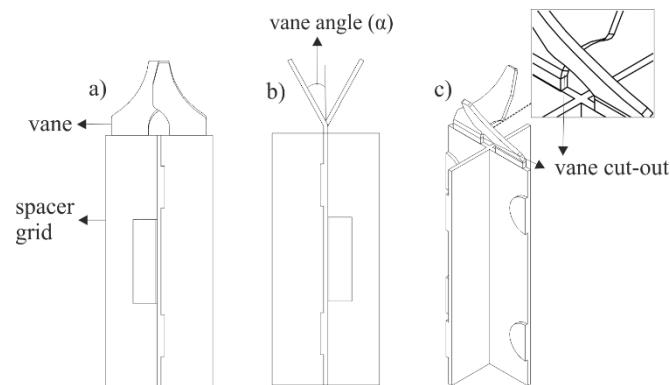
137 As can be seen in Table 1 and Table 2, either the swirl factor, or the mixing coefficient, or the pressure  
 138 drop were taken into account to assess the optimum vane angle. Only very few authors actually  
 139 combined those three parameters (swirl factor, mixing coefficient, pressure drop) in a single study. The  
 140 above literature analysis shows that the following gaps have not yet been bridged:

- 141 – The majority of the studies were done with a vane angle close to  $30 \pm 2^\circ$ . The shape evolution of the  
 142 flow vortex was not yet studied in detail for other vane angles. More insight into the dynamics of the  
 143 vortex formation and its decay downstream of the spacer grid is needed.
- 144 – Further studies on vane design explaining how cross and swirl flows affect the heat transfer are  
 145 needed. A more detailed analysis of cross and swirl flow changes for different vane angles contributes  
 146 to understanding the flow hydrodynamics.
- 147 – Only the studies in References [4, 18, 19] considered the effect of the vane and twist angles. Yet,  
 148 heat transfer was not taken into account except in Reference [18].

149 Analysis of the above state-of-the-art literature also showed, that there still exists a general disagreement  
 150 about the choice for the RANS turbulence model. In this paper, we therefore analyze numerically the  
 151 effect of the vane angle on deformation rate, swirl flow, cross-flow, heat transfer, and pressure drop.

## 152 2. Methods

153 As illustrated in Figure 1, the present study focusses on a vortex generating split type vane arrangement  
 154 since this vane type is the most common one [1-3, 11-12, 25-31]. One sub-channel was modelled to  
 155 investigate the mixing rate. The two inclined vanes in the center of the sub-channel cause the flow  
 156 downstream of the spacer to swirl [16].

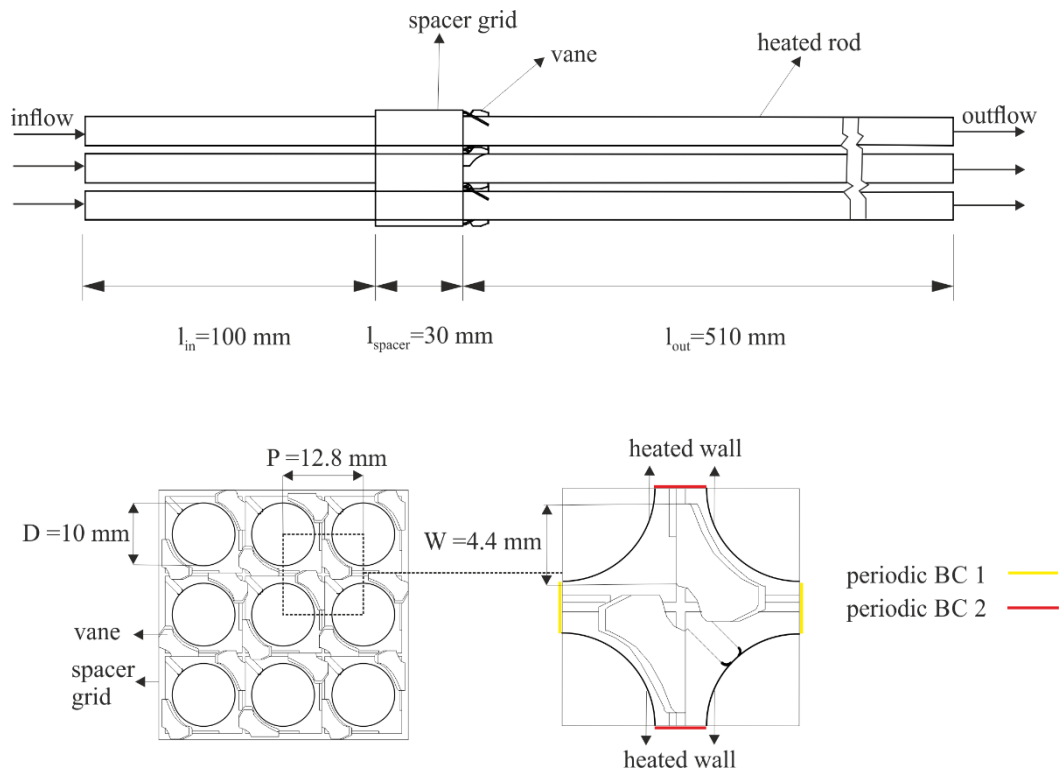


157  
 158 **Figure 1:** Schematic of the investigated grid spacer equipped with two split vanes: a) front view b)  
 159 side view c) cross view.

160 The numerical domain consists of a bounded box containing a  $3 \times 3$  rod arrangement. Each rod has an  
 161 axial extension of 640 mm. A spacer grid is located 100 mm downstream of the inlet. The rod diameter  
 162 is set to  $D = 10$  mm with a bundle pitch set to  $P = 12.8$  mm. The spacer grid has a length of  $l_{\text{spacer}} =$   
 163 30 mm and thickness of 0.5 mm. The flow was simulated for the following six configurations of the  
 164 spacer grid:



- 165 - a rod bundle framed in a spacer grid equipped with no vanes as a reference case,
- 166 - a rod bundle framed in a spacer grid equipped with split vanes, whose angles were set to  $\alpha =$
- 167  $20^\circ, 25^\circ, 29^\circ, 32^\circ,$  and  $40^\circ$ .
- 168 Steady flow simulations were performed using the flow solver ANSYS CFX 18.2. Figure 2 shows a
- 169 schematic of the rod bundle geometry presently used. The boundary conditions were set as follows:
- 170 - uniform heat flux of  $20,000 \text{ W/m}^2$  at rod surfaces,
- 171 - constant atmospheric pressure at outlet,
- 172 - inlet with a temperature of  $290 \text{ K}$ ,
- 173 - inlet with a velocity of  $U = 0.25 \text{ m/s}$ ,
- 174 - inlet turbulence intensity set to  $5 \%$ .



175  
 176 **Figure 2:** Schematic view of 3x3 rod bundle geometry with spacer grid and split type vanes.

177 The Reynolds number was set to  $Re = 14,000$  in all subsequent calculations. Note, that the Reynolds  
 178 number and the surface heat flux are set to relatively low values compared to the nominal ones under  
 179 normal operating conditions. These chosen values enabled us comparative simulations with both a  
 180 suitable mesh resolution near the wall ( $y^+ < 1$ ) and an accurate heat transfer prediction at an affordable  
 181 computational cost. Instead of using wall functions, the flow in near wall region was resolved. A no-slip  
 182 boundary condition was assigned to all walls and periodicity was enforced to the sidewalls of the  
 183 domain. Three different turbulence models were studied (Section 3.1) and eventually the RNG  $k-\epsilon$  model  
 184 was selected. The fluid was incompressible. The convergence criterion was set by making sure the RMS  
 185 residuals fell below  $10^{-6}$  for the continuity, momentum, energy and all turbulent quantities.

## 186 2.1 Governing equations

187 The flow dynamics and the heat transfer are described by the continuity equation

$$\frac{\partial \rho}{\partial t} + \frac{\partial}{\partial x_i}(\rho u_i) = 0, \quad (7)$$

188 the momentum equation

$$\frac{\partial}{\partial t}(\rho u_i) + \frac{\partial}{\partial x_i}(\rho u_i u_j) = -\frac{\partial p}{\partial x_i} + \frac{\partial \tau_{ij}}{\partial x_j} + \rho g_i, \quad (8)$$

$$\tau_{ij} = \mu^* \frac{\partial u_i}{\partial x_j}, \mu^* = \mu + \mu_t, \quad (9)$$

189 and the energy equation

$$\frac{\partial}{\partial t}(\rho c_p T) + \frac{\partial}{\partial x_i}(\rho c_p u_i T) = \frac{\partial}{\partial x_i} \left( \lambda \frac{\partial T}{\partial x_i} \right). \quad (10)$$

190 Where  $\rho$  is the fluid density,  $u_{i=0,1,2}$  is the velocity component in the  $i$ -th direction,  $p$  is the pressure,  
191  $\tau_{ij}$  is the stress tensor,  $c_p$  is the specific heat coefficient,  $\lambda$  is the thermal conductivity,  $\mu^*$  is the total  
192 viscosity,  $\mu$  is the dynamic viscosity,  $\mu_t$  is the turbulent viscosity,  $t$  is the time and  $T$  is the temperature.  
193 These differential equations are solved numerically along the  $x$ ,  $y$  and  $z$  directions. In the present study,  
194 the Shear Stress Transport (SST), the  $k$ - $\varepsilon$  Explicit Algebraic Reynolds Stress Model (EARSM) and the  
195 Re-Normalisation group (RNG) turbulence models were considered.

### 196 2.1.1 Shear Stress Transport (SST) model

197 The SST model [48] takes advantage of the  $k$ - $\varepsilon$  and  $k$ - $\omega$  [49] turbulence models. For the free-stream  
198 flow far from the wall, the model uses the  $k$ - $\varepsilon$  equations and switches to the  $k$ - $\omega$  equations in the near  
199 wall region. The choice for this turbulence model is based on the fact, that the SST turbulence model  
200 supposedly delivers a good prediction of separating flow with large normal strain and strong acceleration  
201 around the split vane regions [37]. With a fine mesh resolution, as is the case here, the  $k$ - $\varepsilon$  and  $k$ - $\omega$   
202 turbulence models are known to exhibit a good performance in estimating the pressure drop and velocity  
203 profiles, yet they do not perform very well in simulating rotational flows because of the absence of a  
204 rotational flow source term in the governing equation [22, 27].

### 205 2.1.2 Explicit Algebraic Reynolds Stress Model (EARSM) model

206 The Explicit Algebraic Reynolds Stress Model [50] is derived from the Reynolds stress transport  
207 equations, which enables the extension of the  $k$ - $\varepsilon$  and baseline turbulence models to better capture the  
208 secondary flow effects. The selection of this model is motivated by the fact that the Reynolds stresses  
209 are solved using the anisotropy tensor given by pressure-strain correlation. The anisotropy tensor is the  
210 solution of an algebraic matrix equation, which depends on the strain and rotation tensors.

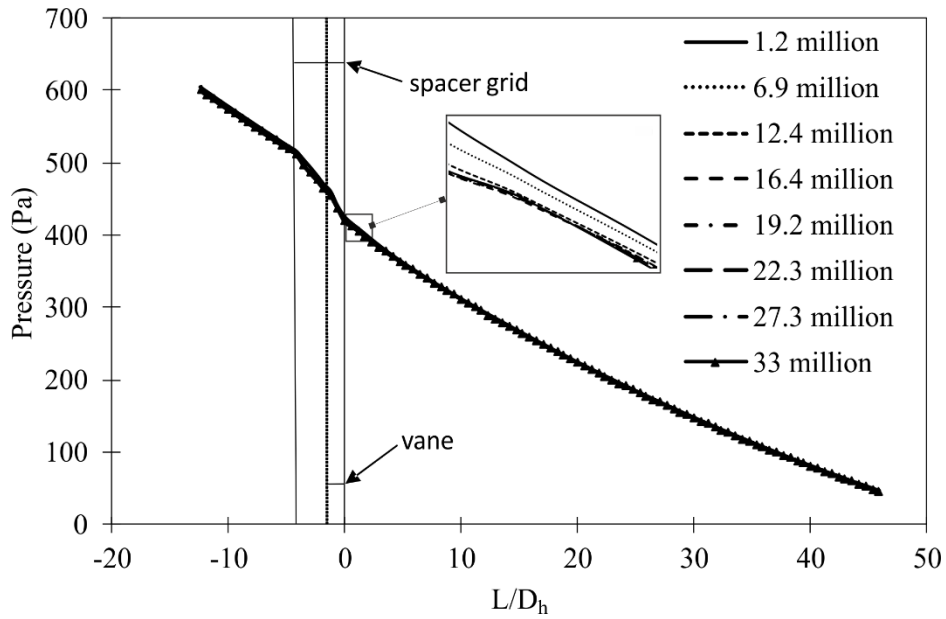
### 211 2.1.3 RNG $k$ -epsilon

212 The RNG  $k$ - $\varepsilon$  model was also selected for this study because it contains an additional term for the  
213 turbulence production and is supposedly better for swirling flows [51].

## 214 2.2 Mesh independence studies

215 Many authors previously used the pressure as convergence indicator in their mesh independence study  
216 [30, 34, 42]. Because the present work involves turbulence and heat transfer, two additional parameters,  
217 namely the turbulent kinetic energy  $k$  and the Nusselt number  $Nu$ , were also used as indicator.  
218 Calculations for the mesh study were done with the RNG  $k$ - $\varepsilon$  model. Figure 3 shows the mean  
219 component of the total static pressure along the axial direction for increasing mesh densities. The

220 simulations were performed with a vane angle set to  $29^\circ$ . It can be seen that the pressure evolution is  
 221 hardly sensitive to the mesh density. We also note that the grid spacer causes a pressure drop of  
 222 approximately 100 Pa.



223

224 **Figure 3:** Effect of grid refinement on the mean component of the total static pressure  $P(L)$ .

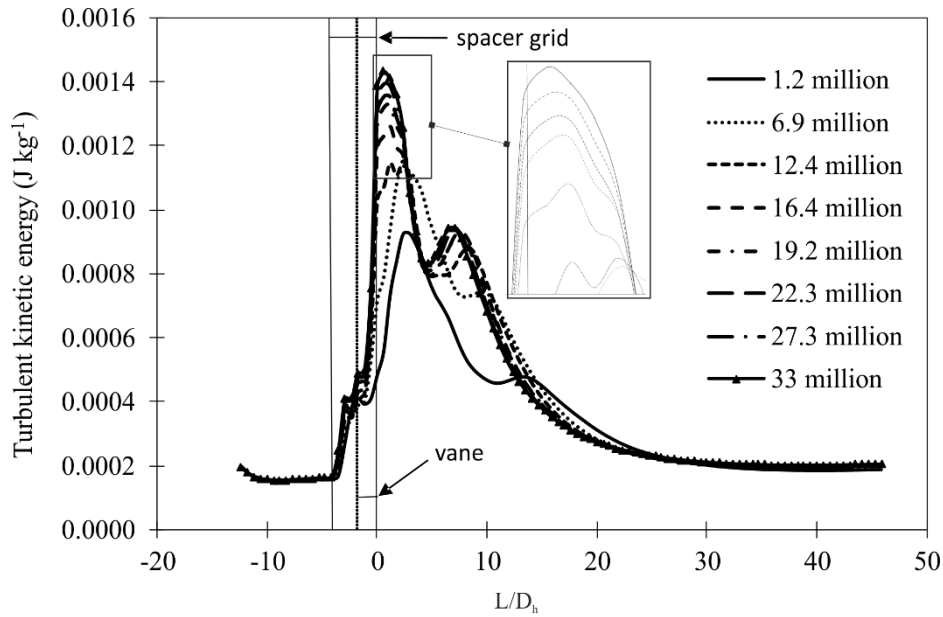
225 A hybrid mesh was used to discretize the flow domain. A tetrahedral mesh near the spacer and the vanes  
 226 was used to account for the large flow anisotropy. In the remaining volume, a hexahedral mesh was  
 227 used. Figure 4 shows exemplarily three different meshes with 6.9 million elements (mesh 1, subfigure  
 228 a), 12.4 million elements (mesh 2, subfigure b), and 33 million elements (mesh 2, subfigure c). Their  
 229 minimum and the maximum mesh size elements are 0.012 mm and 0.26 mm for mesh 1, 0.016 mm and  
 230 0.22 mm for mesh 2, and 0.017 mm and 0.15 mm for mesh 3.

231



232 **Figure 4:** Hybrid meshes with a) 6.9 million, b) 12.4 million, and c) 33 million elements.

233 Figure 5 shows the simulated mean turbulent kinetic energy (TKE) along the axial direction for  
 234 increasing mesh densities. Upstream of to the spacer grid, the mean TKE is very much mesh  
 235 independent. The effect of mesh refinement is largely noticeable within and downstream of the grid  
 236 spacer in the region  $0 < L < 12D_h$ . We also found that a grid with 12.4 million is sufficient.



237

238

**Figure 5:** Effect of grid refinement on the mean turbulent kinetic energy  $k(x)$ .

239

Figure 6 shows the simulated Nusselt number along the axial direction for increasing mesh densities.

240

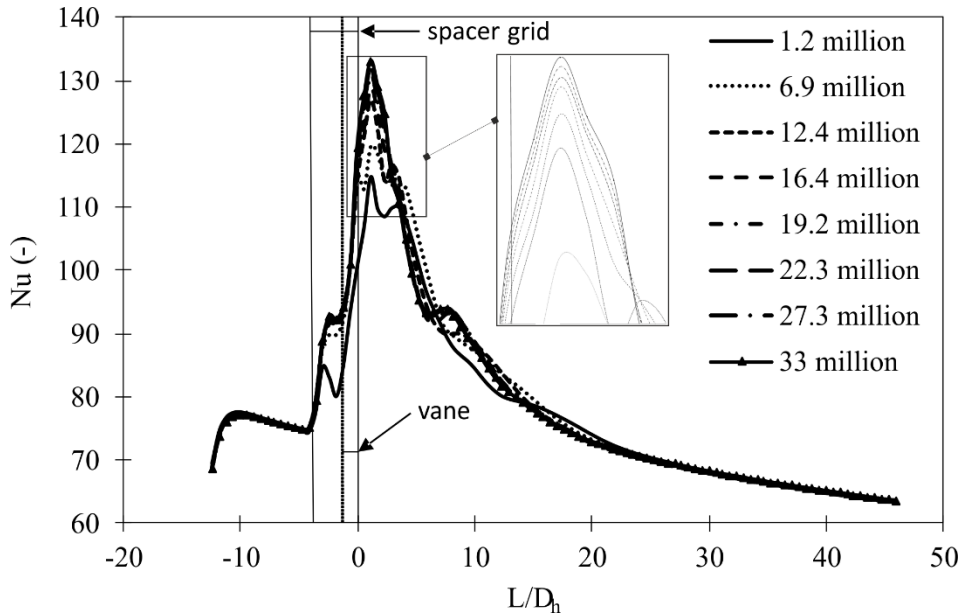
Similarly, the effect of mesh refinement is largely noticeable within and downstream of the spacer grid,

241

in the region  $0 < L < 5D_h$ . It is found, that a minimum number of about  $N=12.10^6$  of grid points is

242

necessary to reach mesh-independency in the axial evolution  $Nu$ .



243

244

**Figure 6:** Effect of grid refinement on the Nusselt number  $Nu(x)$ .

245

Table 3 summarizes the relative change in the integral value of the pressure, the TKE, and  $Nu$ . To reduce

246

the computational effort, all subsequent simulations presented in this work were performed with a grid

247

number set to  $N=12.4 \times 10^6$ , resulting in relative average change below 1% for the pressure, below 3%

248

for the TKE, and below 1% for the Nusselt number.

249

250

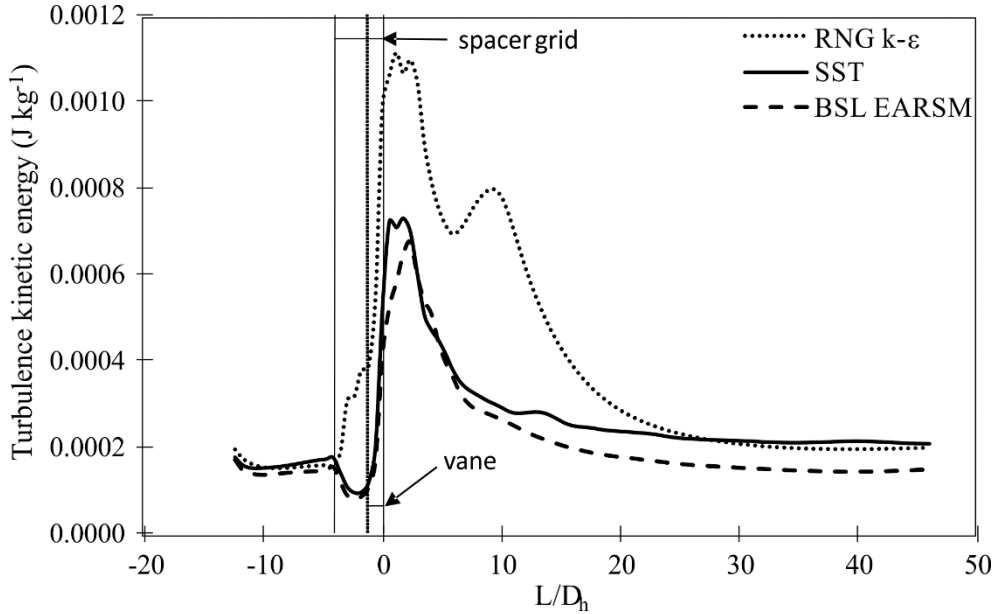
Cell number [ $\times 10^6$ ]	Average relative change		
	TKE [ $\text{J kg}^{-1}$ ]	Nu [-]	Pressure [Pa]
1.2 – 6.9	10.96 %	1.79 %	< 1%
6.9 – 12.4	4.48 %	0.84 %	< 1%
12.4 – 16.4	2.61 %	0.58 %	< 1%
16.4 – 19.2	1.23 %	0.21 %	< 1%
19.2 – 22.3	1.08 %	0.19 %	< 1%
22.3 – 27.3	0.89 %	0.13 %	< 1%
27.3 – 33	0.57 %	0.10 %	< 1%

251 **Table 3:** Effect of grid refinement on the relative change in the integral value of the TKE, Nu, and P.

## 252 3. Results

### 253 3.1 Turbulence model

254 Figure 7 shows the evolution of the TKE, integrated in-plane, as a function of the distance from the  
 255 vane. The TKE evolution was computed for the three selected turbulence models. Upstream of the spacer  
 256 grid in the region  $-12 D_h < L < -3.7 D_h$ , the turbulence model has a negligible effect on the TKE.  
 257 Within and downstream of the spacer grid, that is  $L > -3.7 D_h$ , the SST and the EARSM models  
 258 perform similarly. The results obtained with the RNG k- $\epsilon$  model however show a higher turbulence  
 259 evolution throughout the entire downstream region. A first global maxima at position  $L \approx 1 D_h$  and a  
 260 second maxima further downstream of the spacer at position  $L \approx 10 D_h$  can be observed. The presence  
 261 of a second maxima in the TKE was also reported in the simulations performed by In [20] and by In *et*  
 262 *al.* [46] using a k- $\epsilon$  turbulence model. Beyond the position  $L > 24 D_h$ , all turbulence models lead to a  
 263 simulated TKE reaching a constant plateau.

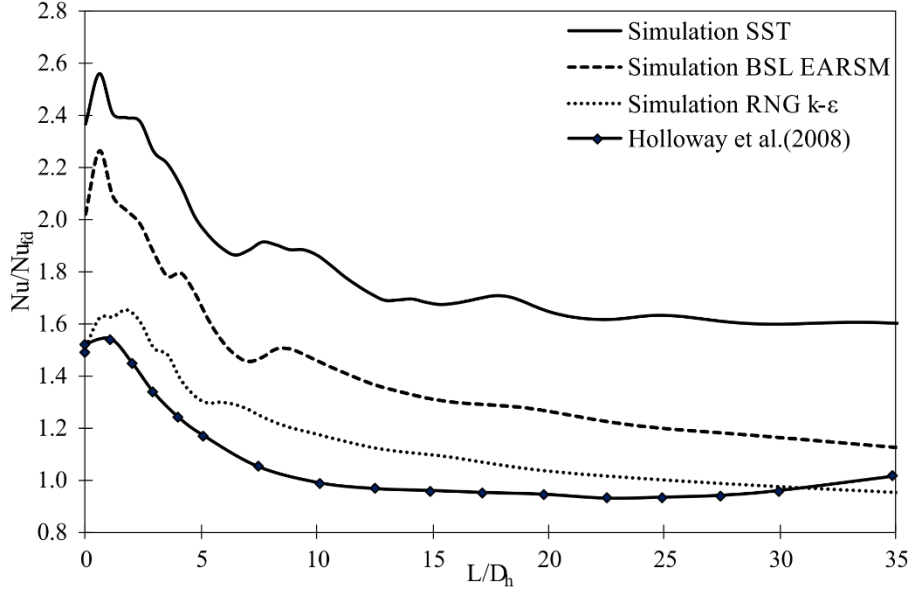


264

265 **Figure 7:** Turbulent kinetic energy distribution along the axial direction for a vane angle of  $29^\circ$ .

266 Published data from two experimental studies performed with split vanes and heated rods are available.  
 267 The first one was performed by Holloway *et al.* [52] with water as coolant fluid. Because the rod had to  
 268 be moved in the axial direction during in these experiments, the liquid flow and the thermal boundary  
 269 layer were somewhat disturbed. Therefore, we decided to use the second experiment by Holloway *et al.*  
 270 [5], in which the rod was fixed and air was the coolant fluid. In order to assess the performance of each  
 271 turbulence model, we compared the simulation results with the experimental results provided by

272 Holloway *et al.* [5]. In their experimental tests, Holloway *et al.* [5] estimated an experimental uncertainty  
 273 of Nusselt number about  $\pm 8.4\%$ . For comparison purposes, the calculations were here repeated at  $Re =$   
 274  $29,000$ . Figure 8 shows the streamwise evolution of the average Nusselt number starting from  $L = 0$ .  
 275 The in-plane averaged Nusselt number  $Nu(L)$  was normalized with the fully developed Nusselt number  
 276 taken at position  $L = 22D_h$  and calculated as  $L_e/D_h = 4.4Re^{1/6}$ .



277

278 **Figure 8:** Evolution of the normalized Nusselt number for  $Re = 29,000$  and a vane angle of  $29^\circ$ .

279 The axial evolution of the normalized Nusselt number shows that all selected turbulence models  
 280 overestimated the experimentally determined Nusselt number. This overestimation is also backed up by  
 281 the RANS simulations performed by Tseng *et al.* [37]. The SST and the EARSM turbulence models had  
 282 here maximum errors estimated at about 84% and 45%, respectively. The findings also show that the  
 283 RNG k-ε turbulence model performed best. It had a maximum error estimated at about 18%.

### 284 3.2 Deformation rate of the flow

285 To better understand the change in the fluid deformation induced by the vanes, the tensor of the velocity  
 286 gradient [53],

$$\nabla \otimes \mathbf{U}|_{ij} = \mathbf{S}_{ij} + \mathbf{\Omega}_{ij} \quad (11)$$

287 with

$$\mathbf{S}_{ij} = \frac{1}{2} \left( \frac{\partial U_i}{\partial x_j} + \frac{\partial U_j}{\partial x_i} \right) \quad (12)$$

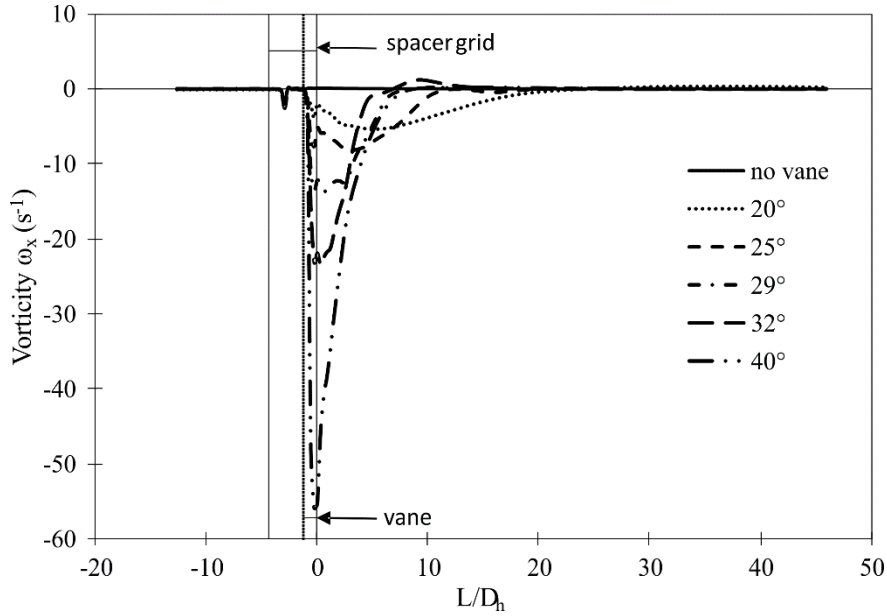
$$\mathbf{\Omega}_{ij} = +\frac{1}{2} \left( \frac{\partial U_i}{\partial x_j} - \frac{\partial U_j}{\partial x_i} \right), \quad (13)$$

288 was calculated for each vane angle. The tensor in Equation 11 is decomposed into a symmetric and an  
 289 asymmetric part, which respectively describe the rate-of-strain  $\mathbf{S}_{ij}$  and the rate-of-rotation  $\mathbf{\Omega}_{ij}$  [54].  $\mathbf{S}_{ij}$   
 290 is a measure of the local folding and stretching of the flow and  $\mathbf{\Omega}_{ij}$  is a measure of the local flow rotation.  
 291 The reason behind separating the tensor  $\nabla \otimes \mathbf{U}$  into a strain and a rotation part is to analyse the role  
 292 played by the viscous stresses  $\tau_{ij}$  (See Eq. 8). In fact, the strain component  $\mathbf{S}_{ij}$  describes the flow motion

293 that resists the viscous stresses, while the rotation component  $\Omega_{ij}$  describes the flow motion that is not  
 294 counteracted by viscous stresses [53]. In the following, the effect of vorticity and strain is analyzed for  
 295 each vane angle.

### 296 3.2.1 Vorticity

297 The vorticity vector  $\boldsymbol{\omega} = [\omega_x \ \omega_y \ \omega_z]^T = [\Omega_{xx} \ \Omega_{yy} \ \Omega_{zz}]^T$  is defined using the diagonal components of  
 298 rate-of-rotation tensor in Eq. 13. Results from the present simulations show that the magnitude of the  
 299 axial component  $|\omega_x|$  is up to eight times greater than the other two component magnitudes  $|\omega_y|$  and  
 300  $|\omega_z|$ . Figure 9 illustrates the evolution of the mean x-component of the vorticity in the axial direction of  
 301 the rod.



302

303 **Figure 9:** Axial component of vorticity distribution along the axial direction for different vane angles  
 304 and no vane.

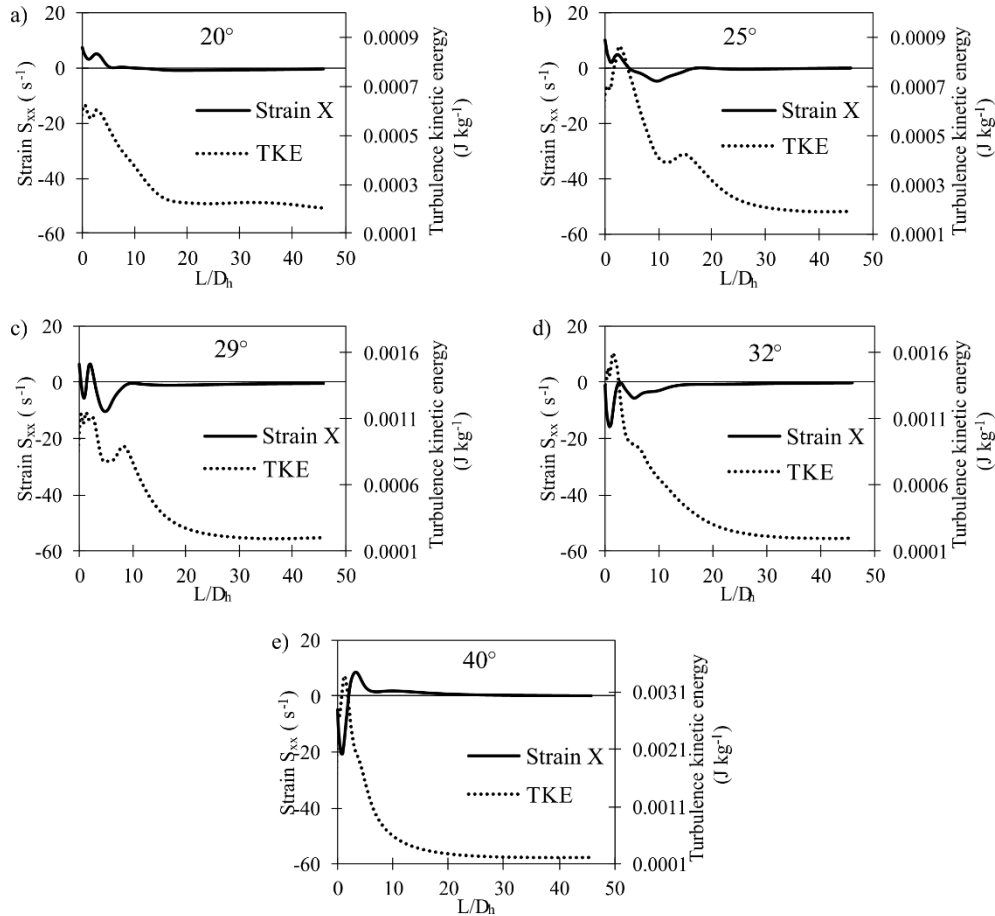
305 The spacer grid without the vanes causes a low vorticity throughout the entire sub-channel. In the  
 306 presence of vanes, the vorticity reaches a maximum downstream of the spacer grid and eventually  
 307 decreases to zero. With a 20° vane angle, the maximum vorticity is about  $\omega_x = -5 \text{ s}^{-1}$  at a position  
 308 around  $L = 5.5 D_h$  and it becomes zero further downstream at around  $L = 19 D_h$ . With a 40° vane angle,  
 309 the maximum vorticity is about  $\omega_x = -55 \text{ s}^{-1}$  at a position around  $L = 0$  and reached a zero value  
 310 further downstream at around  $L = 10 D_h$ . The present results also show that the maximum vorticity  
 311 increases with the vane angle. When the vane angle rises from 20° to 40°, the maximum vorticity  
 312 increases by up to a factor 10. The axial length, over which the flow is rotational, however, decreases  
 313 with the vane angle. There exists an optimum vane angle, for which a trade-off between vorticity  
 314 magnitude and axial length, is achieved.

### 315 3.2.2 Strain

316 The vanes produce a certain amount of shear strain rate resulting in deformation of the vortex  
 317 downstream of the spacer grid. Strain and vorticity are the two main mechanisms responsible for the  
 318 transfer of energy from the mean flow to the turbulence field. The production of turbulent energy is  
 319 function of the strain rate  $S_{ij}$  and the turbulent velocity fluctuations. The production tensor is defined as  
 320 [505]

$$P_{ij} = -\rho \overline{u_i u_j} S_{ij}. \quad (14)$$

321 The axial evolution of the average strain rate  $S_{xx}$ , characterizing the deformation rate of the vortex by  
 322 flow shearing in the  $yz$ -plane normal to the axial flow direction, is analysed. This tensor component is  
 323 here of practical interest. Figure 10 compares the axial component of strain  $S_{xx}$  with the turbulent kinetic  
 324 energy  $k$  along the axial direction downstream of the spacer grid. It can be seen that the peak in the  
 325 turbulent kinetic energy roughly coincides with the peak also observed for the strain  $S_{xx}$ . The strain  
 326 effect disappears for all vane angles beyond about  $L > 15 D_h$ . The results shown in Figure 10 are in line  
 327 with Eq. (12). A higher strain results in a higher turbulent kinetic energy.  $29^\circ$  and  $32^\circ$  vane angles result  
 328 in an improved shear deformation rate since the magnitude and effective length of strain have a better  
 329 combination than other vane angles.



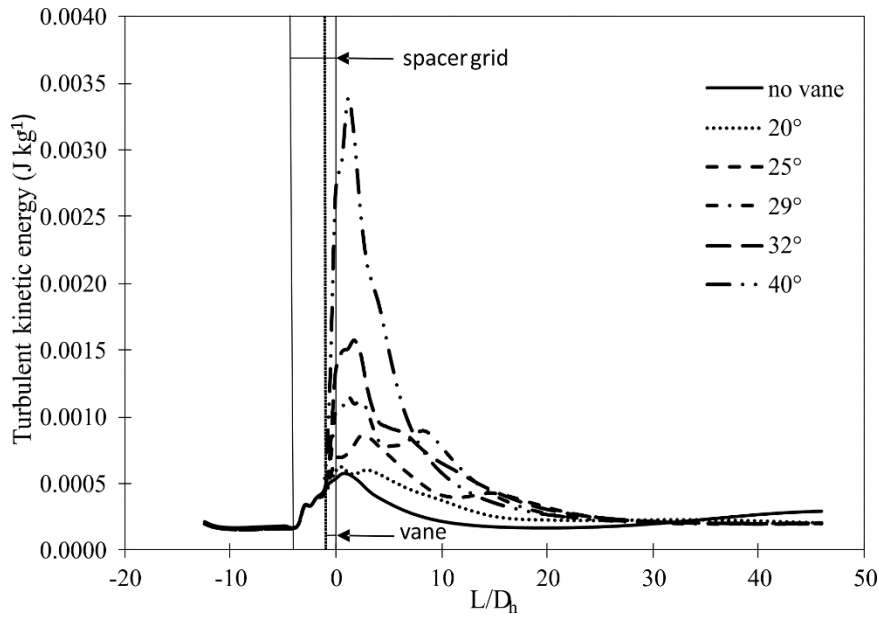
330

331 **Figure 10:** Axial component of the strain component  $S_{xx}$  and turbulent kinetic energy distribution  
 332 along the axial direction for vane angles a)  $20^\circ$  b)  $25^\circ$  c)  $29^\circ$  d)  $32^\circ$  e)  $40^\circ$ .

### 333 3.2.3 Turbulent kinetic energy

334 Figure 11 shows the axial evolution of the turbulent kinetic energy, averaged in the  $yz$ -plane for each  
 335 vane angle. Upstream of the vane, the TKE is hardly affected by the vane angle. The difference in the  
 336 TKE evolution becomes noticeable when the coolant starts passing through the vanes. The effect of the  
 337 vane angle of TKE closely resembles of the vorticity. The magnitude of the maxima increases with the  
 338 vane angle while the axial length, over which the flow is highly turbulent, decreases with the vane angle.  
 339 There exists an optimum vane angle with respect to straight of between high turbulent intensity and  
 340 adequate axial length.





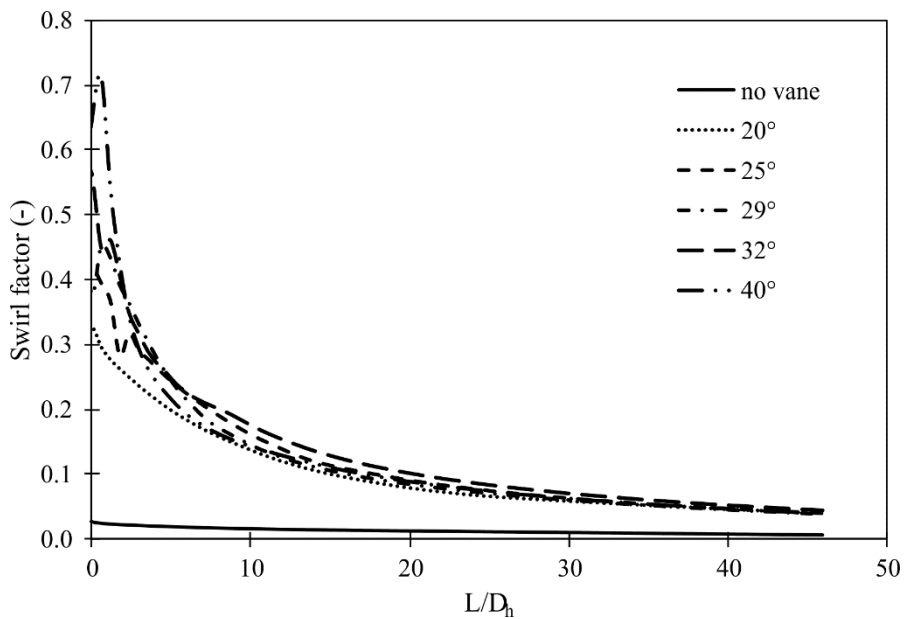
341

342

**Figure 11:** Axial evolution of the turbulent kinetic energy averaged in the yz-plane.

343 **3.3 Secondary flow**

344 The secondary flow, induced by the vanes and gradually decreasing downstream of the spacer grid, is  
 345 here investigated. To assess the secondary flow quantitatively, the swirl factor was calculated as a  
 346 function of the streamwise length  $L$  (See Eq. 5). Figure 12 shows the swirl factor along the downstream  
 347 axis of the spacer grid. Very little flow swirl is observed for the no vane case. For vane angles above  
 348  $20^\circ$ , the swirl factor decreases exponentially with the length  $L$ . The swirl factor is lowest for  $20^\circ$   
 349 vane angle. Up to position  $L = 2.3D_h$ , the swirl factor is highest for  $40^\circ$  vane angle. In the intermediate range  
 350  $2.3D_h < L < 4.5D_h$ , the swirl factor is highest for  $29^\circ$  vane angle, closely followed by  $32^\circ$  vane angle.  
 351 Beyond  $L > 8D_h$ , the swirl factor is highest for  $32^\circ$  vane angle downstream the vane. The vane angle  
 352  $32^\circ$  has the lowest swirl factor throughout.

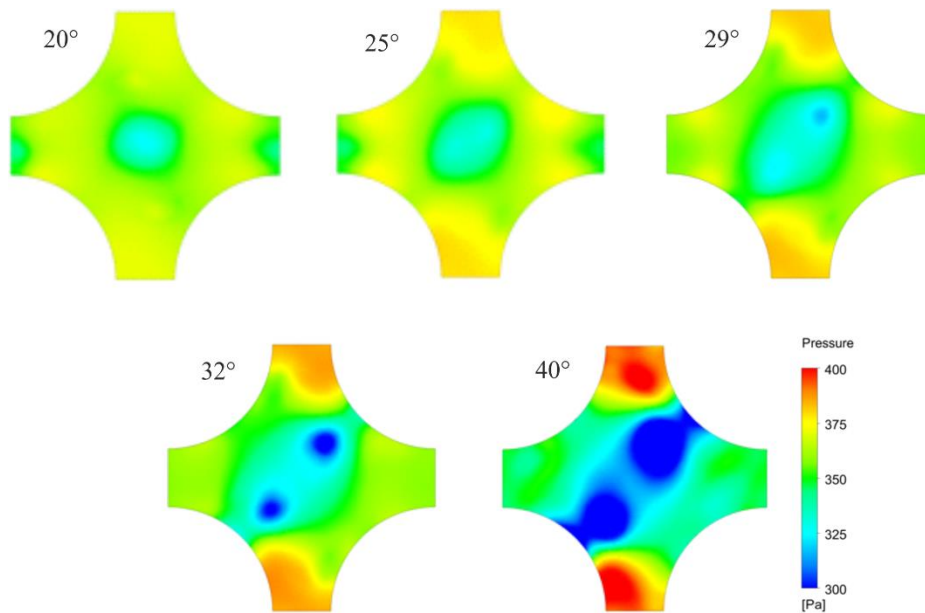


353

354

**Figure 12:** Axial variation of the swirl factor with increasing vane angle.

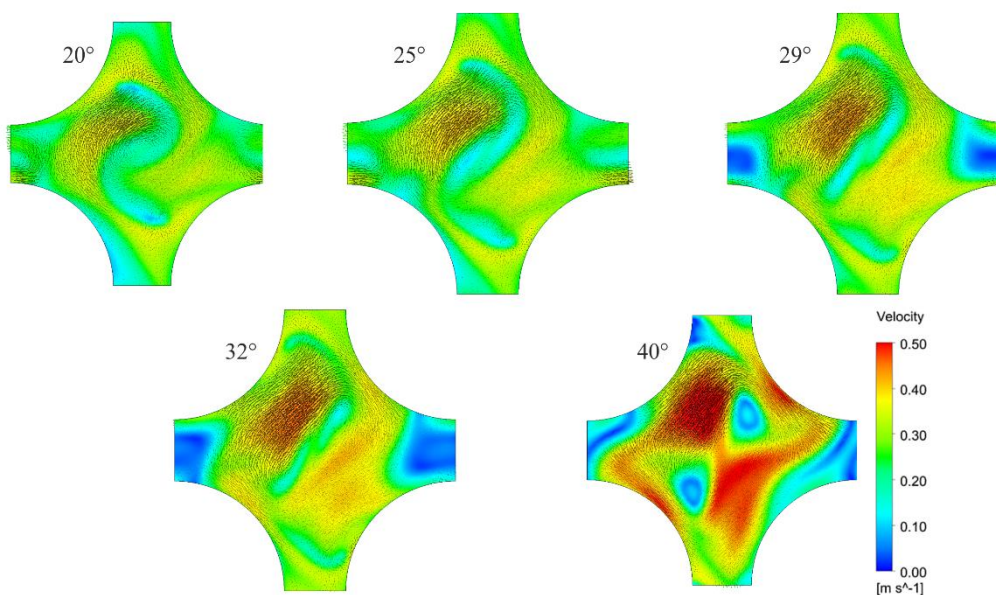
355 Figure 13 shows the cross-sectional pressure field at position  $L = 0$  for each vane angle. As the fluid  
 356 passes through the vanes, it causes a pressure modification in the yz-plane. This modified pressure field  
 357 in-turn results in a flow vortex centered in the sub-channel.



358

359 **Figure 13:** In-plane pressure distribution at  $L = 0$  for vane angles.

360 As can be seen in Figure 14, right upstream of the vanes, the cross-sectional velocity field exhibits a  
 361 characteristic S-shape with an inside velocity that is much lower than outside velocity. The maximum  
 362 velocity approaches 0.35 m/s for the 29° vane angle. As the vane angle increases, the vortex region  
 363 elongates. The maximum fluid velocity rises to 0.5 m/s for a 40° vane angle. Caution should however  
 364 be given to the configuration involving the 40° vane angle. A low-pressure region exists in the boundary  
 365 layer starting from this cut-out part of the vane. Consequently, flow separation occurs due to adverse  
 366 pressure gradients. The blue low velocity regions in the core region of the sub-channel in Figure 14  
 367 illustrates the flow separation occurring for the 40° vane angle.



368

369 **Figure 14:** In-plane velocity distribution at  $L = 0$  for vane angles.

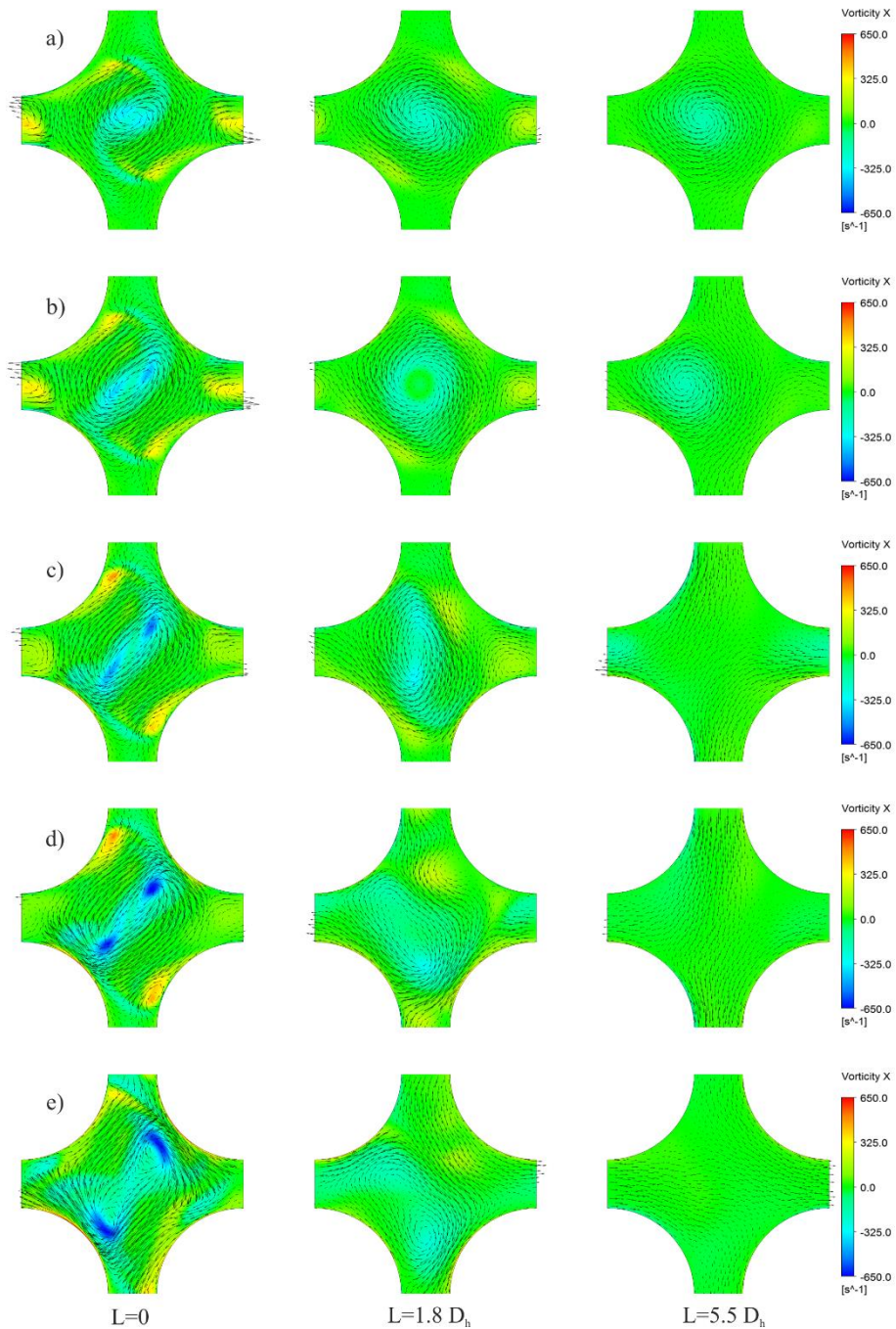
370 Figure 15 represents the secondary flow velocity fields in three successive cross-sectional planes located  
371 at positions  $L = 0, 1.8D_h$ , and  $5.5D_h$ . It shows the flow field development for each vane angle.

372 For the  $20^\circ$  vane angle, an elongated circular vortex exists just downstream of the spacer grid at  
373 position  $L = 0$ . The left/right vane pattern creates a clockwise-rotating vortex region with negative  
374 vorticity at the centre of the sub-channel. Beside a dominant swirl flow superimposed with a slight cross-  
375 flow also exists. At position  $L = 1.8D_h$  the swirl flow still persists. The magnitude of the cross-flow  
376 decreases and a small circulation region in the centre of the sub-channel can be seen. At position  $L =$   
377  $5.5D_h$ , the centre of the vortex region migrates away from the sub-channel center. This movement  
378 positively affects the heat transfer from rod surfaces. On the other hand, other rod surfaces that are  
379 further away from the vortex region are negatively affected in terms of the heat transfer due to a  
380 decreasing mixing in this local region.

381 For the  $25^\circ$  vane angle, the vortex is more elongated at position  $L = 0$  and a stronger vorticity is  
382 observed. At around  $L = 1.8D_h$ , a circular flow vortex and a circulation region appear in the sub-  
383 channel. At around  $L = 5.5D_h$ , the circular flow vortex moves to the left of the geometric center of the  
384 sub-channel. The migrated offset position of the vortex center is larger than that observed with the  $20^\circ$   
385 vane angle.

386 For the  $29^\circ$  vane angle, a vortex of nearly rectangular shape forms at position  $L = 0$ . The strength of the  
387 vorticity is higher than for  $25^\circ$  vane angle. At this vary position, there are also smaller re-circulation  
388 regions of positive vorticity near the rods. At around  $L = 1.8D_h$ , the vortex becomes more oval in shape  
389 and migrates further leftwards from the geometric center of the sub-channel. This, in-turn, provides a  
390 better cross-flow. At around  $L = 5.5D_h$ , the vortex disappears and almost no more swirl flow can be  
391 observed. The cross-flow contributes here to an enhanced heat transfer than that obtained for the  $20^\circ$   
392 and  $25^\circ$  vane angles. The lateral velocities also have higher magnitudes near the horizontal and vertical  
393 openings.

394



395

396 **Figure 15:** Axial vorticity fields and lateral velocity vectors for three different cross sections and vane  
 397 angles a) 20° b) 25° c) 29° d) 32° e) 40°.

398 For the 32° vane angle, there exists a rectangular vortex at position  $L = 0$ . It covers a large area of the  
 399 sub-channel cross-section. In this region, there are also two local high vorticity spots reaching high  
 400 negative values. This dominant swirl flow prevents an effective cross-flow. Small flow re-circulations  
 401 similar to 29° vane angle also are also present. At around  $L = 1.8D_h$ , the rectangular vortex becomes  
 402 smaller and migrates to the side. This promotes a better cross-flow within the sub-channel. At around  
 403  $L = 5.5D_h$ , an uneven cross-flow distribution can be observed.

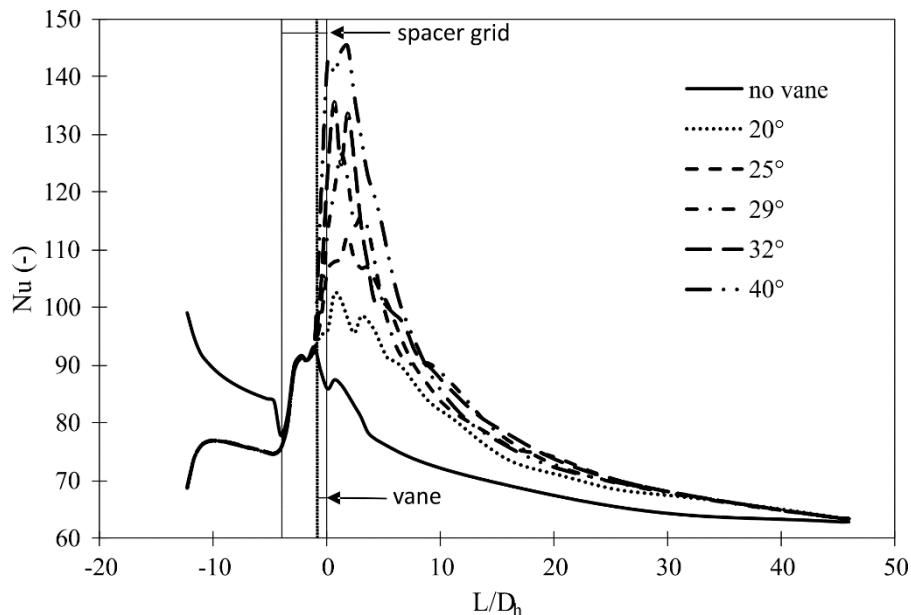
404 For the 40° vane angle, a dominant swirl flow occurs and it covers nearly the entire sub-channel at  
 405 position  $L = 0$ . There are also two small vortices embedded in the large vortex region. In addition, the  
 406 small re-circulation regions near the rod surfaces nearly disappear. At around  $L = 1.8D_h$ , these two

407 small vortices move close to each other and migrate further bottom left of the sub-channel. At  
 408 position  $L = 5.5D_h$ , the swirl flow disappears completely. This also causes an uneven cross-flow  
 409 distribution.

410 Consequently, just after the vanes, strong swirl flow and weak cross-flow are present. As the vane angle  
 411 increases, the vortex region directly downstream of the spacer grid changes in shape. At positions  $L =$   
 412  $0$  and  $L = 1.8D_h$ , there is a strong swirl flow for all angles. The magnitude of the swirl flow decays  
 413 with the axial length  $L$ . There is also a vortex in the sub-channel at position  $L = 5.5D_h$  for the vane angle  
 414  $20^\circ$  and  $25^\circ$ . Yet, at this same position, this vortex region disappears for vane angles  $29^\circ$ ,  $32^\circ$  and  $40^\circ$ .  
 415 As the flow develops, the vortices tend to migrate leftwards from the geometric centre of the sub-  
 416 channel. Holloway *et al.* [25] also observed a similar vortex migration in their experiments. This is  
 417 contrary to their CFD results, which predicted a vortex in the geometric centre of the sub-channel. From  
 418 the present results, we found that the  $29^\circ$  and  $32^\circ$  vane angles provide better cross and swirl flows, which  
 419 are beneficial for an efficient heat transfer.

### 420 3.4 Heat transfer

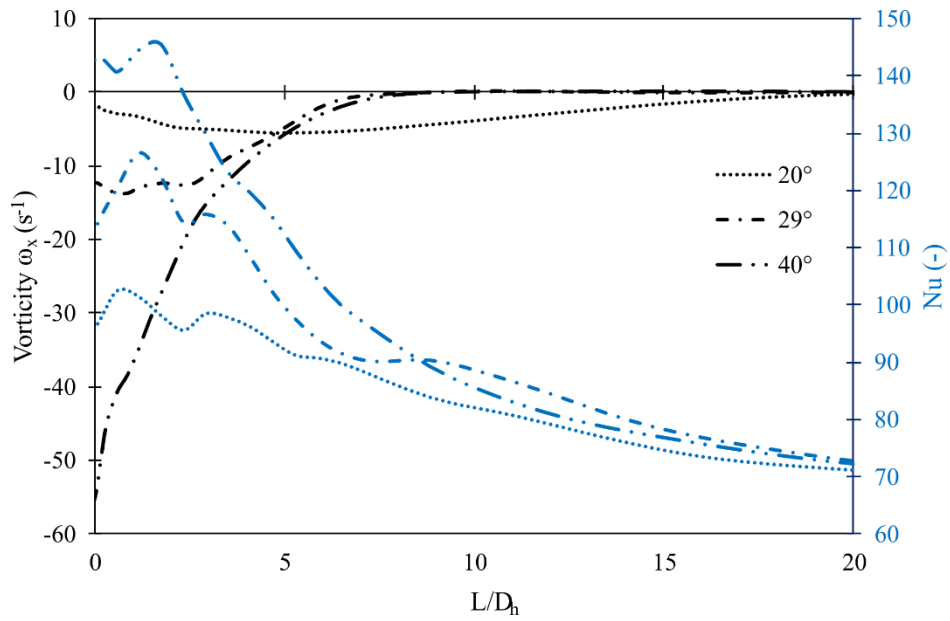
421 Figure 16 illustrates the effect of the vane angle on the axial evolution of Nusselt number. It can be seen,  
 422 that upstream of the spacer grid the vane angle has virtually no effect on the heat transfer. Right  
 423 downstream of the spacer grid, the Nusselt number reaches maxima and eventually decreases  
 424 exponentially with the length  $L$ . A higher vane angle results in a higher maximum. Compared to the no-  
 425 vane configuration, a vane angle of  $20^\circ$ ,  $25^\circ$ ,  $29^\circ$ ,  $32^\circ$  and  $40^\circ$  results in an increase of the average  
 426 Nusselt number downstream of the spacer grid ( $0 < L < 46D_h$ ) of about 7.8%, 10.9%, 12.3%, 13.6%,  
 427 and 15.5% respectively. With a  $40^\circ$  vane angle and in the region  $0 < L < 8D_h$ , the Nusselt number is  
 428 greater than anyone for a smaller vane angle. The Nusselt number evolution obtained with the  $40^\circ$  vane  
 429 angle drops almost to the same level as for  $29^\circ$  vane angle at around  $L = 10D_h$ . The overall decay in the  
 430 Nusselt number exhibits a trend similar to that reported earlier for the turbulent kinetic energy.



431

432 **Figure 16:** Effect of the vane angle on the axial evolution of Nusselt number.

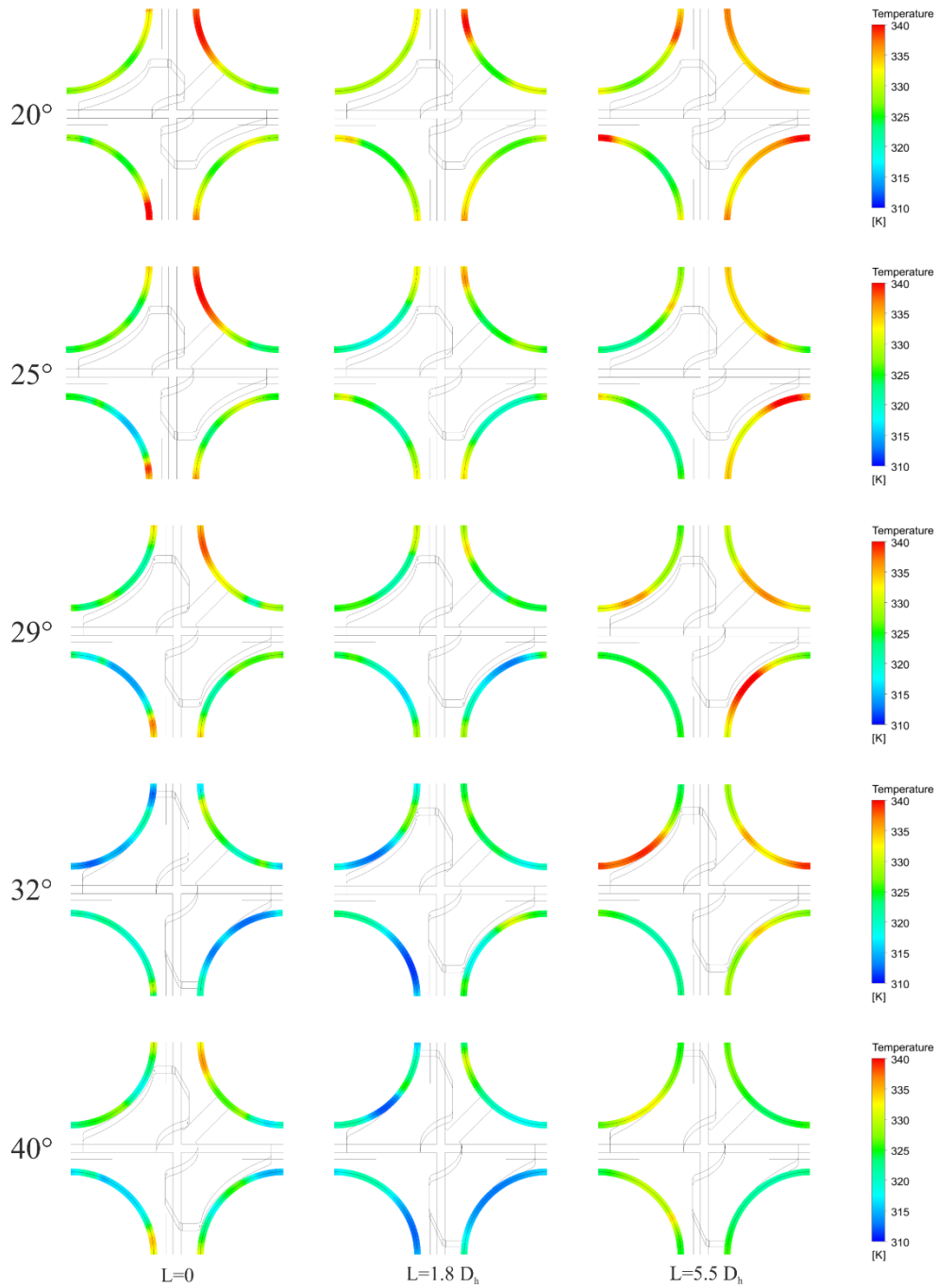
433 An overlay of the flow vorticity with the Nusselt number is shown in Figure 17 for the vane angles  $\alpha =$   
 434  $20^\circ$ ,  $29^\circ$  and  $40^\circ$ . Only three angle were deliberately picked to not overload the figure with information.  
 435 Results from this figure suggests, that heat transfer increases with the flow vorticity in the region  $L <$   
 436  $8D_h$ .



437

438 **Figure 17:** Axial evolution of Nusselt number versus vorticity for vane angles 20°, 29° and 40°.

439 Figure 18 shows the circumferential cross-sectional temperature distribution at three axial positions  $L =$   
 440  $0, 1.8 D_h,$  and  $5.5 D_h$ . At  $L = 0$ , high temperature regions tend to disappear with increasing vane angle.  
 441 With the exception of the 20° vane angle, the surface temperatures at position  $L = 1.8 D_h$  are  
 442 comparatively low. Further downstream, at position  $L = 5.5 D_h$ , high temperature regions occur for  
 443 almost every vane angle. The results hence show that a higher vane angles results in a more  
 444 homogeneous and efficient heat removal.



445

446

**Figure 18:** Circumferential cross-sectional temperature distribution at three axial positions.

447

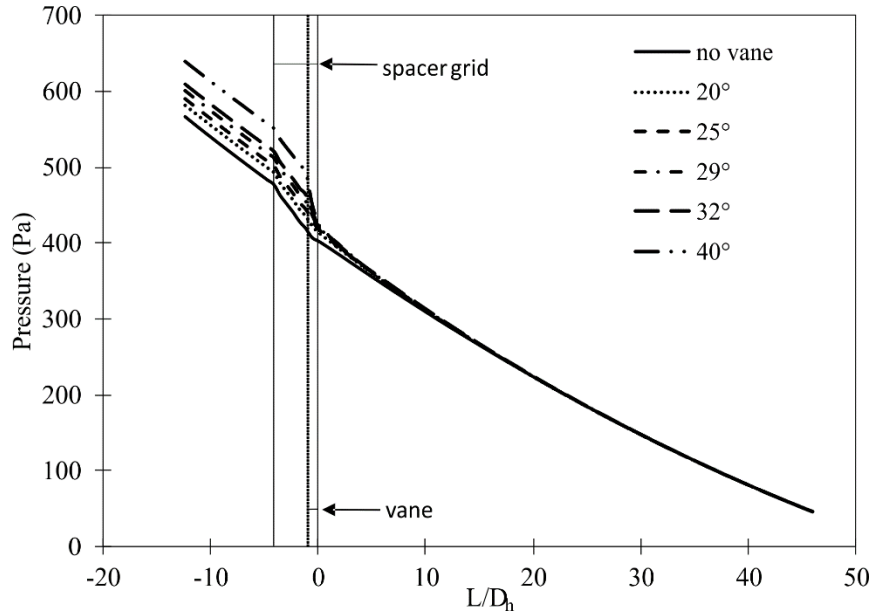
### 3.5 Pressure drop

448

Pressure drop is another important engineering parameter for selecting the most appropriate vane angle.

449

Figure 19 shows the total static pressure distribution in the axial direction for each vane angle.



450

451

**Figure 19:** Effect of vane angle on pressure evolution

452 Upstream of the spacer grid the spacer without vanes leads to the lowest pressure and the spacer grid  
 453 with a 40° vane angle leads to the highest pressure. For the intermediate vane angles, a higher vane angle  
 454 generally results in a higher pressure. The spacer grid and the vanes are known to cause an increase in  
 455 the pressure drop [20, 30]. The present results suggest a considerable pressure drop in the region  
 456  $-4D_h < L < 0$ . Further downstream, that is beyond  $L > 5.5D_h$ , the low axial decrease in the pressure  
 457 is roughly identical for all vane angles. The spacer grid was found to contribute by far to the total  
 458 pressure drop. Table 4 shows the increase in the pressure drop, calculated as  $\Delta P = |P(L/D_h = 0) -$   
 459  $P(L/D_h = -3.7)|$ , as a function of the vane angle. The reference pressure drop is calculated using the  
 460 no-vane simulation.

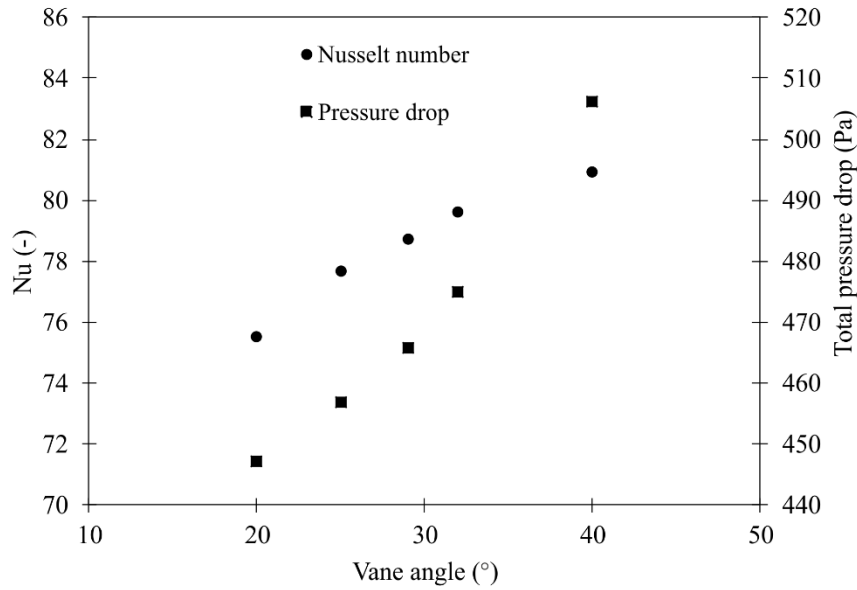
Angle	Pressure drop $\Delta P$ (Pa)	$\Delta P$ Increase (%) $ \Delta P_2 - \Delta P_1 /\Delta P_{\text{ref}}$
No vane (Reference)	$\Delta P_{\text{ref}} = 68.33$	Reference
20°	76.05	11.2 %
25°	80.39	17.6 %
29°	88.64	29.7 %
32°	95.86	40.2 %
40°	122.72	79.6 %

461

**Table 4:** Pressure difference between spacer grid inlet and just after the vanes.

462 Figure 20 shows the Nusselt number averaged over the area  $-3.7 < L/D_h < 46$  as well as the pressure  
 463 drop, calculated as  $\Delta P = |P(L/D_h = -3.7) - P(L/D_h = 46)|$  against the vane angle. It can be seen  
 464 that both the averaged Nusselt number and the pressure drop increase with the vane angle. Care should  
 465 however be taken for larger vane angles. As previously discussed, a 40° vane angle results in flow  
 466 separation. Thus, although a vane angle of 40° provides maximum average heat transfer there is a  
 467 considerable pressure drop caused by the flow separation.





468

469 **Figure 20:** Nusselt number averaged over the area  $-3.7 < L/D_h < 46$  as well as the pressure drop,  
 470 calculated as  $\Delta P = |P_{L/D_h=-3.7} - P_{L/D_h=46}|$ , against vane angle.

#### 471 **4. Conclusions**

472 A substantial state-of-the art review was provided in the beginning of this work and showed, that there  
 473 is no agreed turbulence model for simulations of flow in sub-channel with spacer grid. Besides, most of  
 474 the available studies did not consider flow development and heat transfer related to vane angle. Based  
 475 on the available experimental and numerical studies, we performed numerical studies to elucidate the  
 476 effect of the vane angle on various important key parameters, namely pressure drop, heat transfer, cross-  
 477 flow and flow deformation. Findings from this numerical study can be summarized as follows:

- 478 1. The turbulent kinetic energy and the Nusselt number are decisive parameters and should be  
 479 accounted for in the mesh convergence study.
- 480 2. Among the tested three turbulence models, the RNG k- $\epsilon$  model predicts the heat transfer most  
 481 accurately.
- 482 3. Vorticity is not the only mechanism responsible for enhanced heat transfer downstream of the  
 483 vane. Yet, it has a dominant effect in the region near the vane tip.
- 484 4. The shape and the center of the flow vortex downstream of the vane is a function of the vane  
 485 angle. Irrespective of the vane angle, the vortex eventually migrates away from the sub-channel  
 486 center. Some parts of the rod surfaces are hotter, which in-turn leads to an inhomogeneous heat  
 487 transfer distribution in the sub-channel.
- 488 5. The swirl flow is very strong right downstream of the spacer grid. Swirl and cross flows result  
 489 in highest heat transfer for 29 and 32° vane angles.
- 490 6. For 40° vane angle multiple flow vortices develop and create high pressure drop.
- 491 7. The 29 and 32° vane angles give a better heat transfer performance in terms of average cross  
 492 sectional Nusselt number. Higher vane angle results in a more uniform temperature distribution  
 493 on the rod surfaces.

494 The above results are quantitatively summarized in Table 5. Since the flow in the sub-channel is a  
 495 developing flow, not only the local mixing and heat transfer efficiency but also the continuity and  
 496 balance of these efficiencies along the whole sub-channel must be taken into account. In this context, it  
 497 noticeable that a vane angle close to 30° provides a good trade-off between flow deformation, which

498 affects the mixing efficiency, the secondary flow, the heat transfer, and the pressure loss. An optimal  
 499 heat transfer due to efficient cross-flow from one sub-channel to another is also achieved.

Vane angle	20°	25°	29°	32°	40°
Measure of mixing efficiency	o	+	+++	+++	+
Secondary cross-flow efficiency	o	++	+++	+++	+
Swirl flow	o	++	++	+++	++
Heat transfer efficiency	o	+	++	++	+++
Pressure loss	o	+	++	++	+++
Note					flow separation

500 **Table 5:** Effect of vane angle on the different hydrodynamic and heat transfer parameters (o low  
 501 effect, + moderate effect, ++ strong effect, +++ extreme effect).

## 502 5. References

- 503 1. Chang, S.K., et al., *Phenomenological investigations on the turbulent flow structures in a rod*  
 504 *bundle array with mixing devices*. Nuclear Engineering and Design, 2008. **238**(3): p. 600-609.
- 505 2. Chang, S.K., S. Kim, and C.H. Song, *Turbulent mixing in a rod bundle with vaned spacer*  
 506 *grids: OECD/NEA-KAERI CFD benchmark exercise test*. Nuclear Engineering and Design,  
 507 2014. **279**: p. 19-36.
- 508 3. Wang, X.Y., et al., *Flow visualization and mixing quantification in a rod bundle using laser*  
 509 *induced fluorescence*. Nuclear Engineering and Design, 2016. **305**: p. 1-8.
- 510 4. Shen, Y.F., Z.D. Cao, and Q.G. Lu, *An Investigation of Cross-Flow Mixing Effect Caused by*  
 511 *Grid Spacer with Mixing Blades in a Rod Bundle*. Nuclear Engineering and Design, 1991.  
 512 **125**(2): p. 111-119.
- 513 5. Holloway, M.V., D.E. Beasley, and M.E. Conner, *Single-phase convective heat transfer in rod*  
 514 *bundles*. Nuclear Engineering and Design, 2008. **238**(4): p. 848-858.
- 515 6. Byun, S.J., et al., *Experimental study on the heat transfer enhancement in sub-channels of 6 x*  
 516 *6 rod bundle with large scale vortex flow mixing vanes*. Nuclear Engineering and Design,  
 517 2018. **339**: p. 105-115.
- 518 7. In, W.K., C.H. Shin, and C.Y. Lee, *Convective heat transfer experiment of rod bundle flow*  
 519 *with twist-vane spacer grid*. Nuclear Engineering and Design, 2015. **295**: p. 173-181.
- 520 8. Moon, S.K., et al., *Single-phase convective heat transfer enhancement by spacer grids in a*  
 521 *rod bundle*. Journal of Nuclear Science and Technology, 2014. **51**(4): p. 543-557.
- 522 9. Han, S.Y., et al., *Measurements of the flow characteristics of the lateral flow in the 6 x 6 rod*  
 523 *bundles with Tandem Arrangement Vanes*. Nuclear Engineering and Design, 2009. **239**(12): p.  
 524 2728-2736.
- 525 10. Caraghiaur, D., H. Anglart, and W. Frid, *Experimental investigation of turbulent flow through*  
 526 *spacer grids in fuel rod bundles*. Nuclear Engineering and Design, 2009. **239**(10): p. 2013-  
 527 2021.
- 528 11. Ikeda, K., *CFD application to advanced design for high efficiency spacer grid*. Nuclear  
 529 Engineering and Design, 2014. **279**: p. 73-82.
- 530 12. McClusky, H.L., et al., *Mapping of the lateral flow field in typical subchannels of a support*  
 531 *grid with vanes*. Journal of Fluids Engineering-Transactions of the Asme, 2003. **125**(6): p.  
 532 987-996.
- 533 13. Xiong, J.B., et al., *Experimental investigation on anisotropic turbulent flow in a 6 x 6 rod*  
 534 *bundle with LDV*. Nuclear Engineering and Design, 2014. **278**: p. 333-343.
- 535 14. Qu, W.H., et al., *High-fidelity PIV measurement of cross flow in 5 x 5 rod bundle with mixing*  
 536 *vane grids*. Nuclear Engineering and Design, 2019. **344**: p. 131-143.
- 537 15. Bhattacharjee, S., G. Ricciardi, and S. Viazzo, *Comparative study of the contribution of*  
 538 *various PWR spacer grid components to hydrodynamic and wall pressure characteristics*.  
 539 Nuclear Engineering and Design, 2017. **317**: p. 22-43.
- 540 16. Kim, K.Y. and J.W. Seo, *Numerical optimization for the design of a spacer grid with mixing*  
 541 *vanes in a pressurized water reactor fuel assembly*. Nuclear Technology, 2005. **149**(1): p. 62-  
 542 70.

- 543 17. Cui, X.Z. and K.Y. Kim, *Three-dimensional analysis of turbulent heat transfer and flow*  
544 *through mixing vane in a subchannel of nuclear reactor*. Journal of Nuclear Science and  
545 Technology, 2003. **40**(10): p. 719-724.
- 546 18. Wu, J.M., et al., *CFD analysis of the impact of a novel spacer grid with longitudinal vortex*  
547 *generators on the sub-channel flow and heat transfer of a rod bundle*. Nuclear Engineering  
548 and Design, 2017. **324**: p. 78-92.
- 549 19. Cheng, S.H., H.D. Chen, and X.Y. Zhang, *CFD analysis of flow field in a 5 x 5 rod bundle*  
550 *with multi-grid*. Annals of Nuclear Energy, 2017. **99**: p. 464-470.
- 551 20. In, W.K., *Numerical study of coolant mixing caused by the flow deflectors in a nuclear fuel*  
552 *bundle*. Nuclear Technology, 2001. **134**(2): p. 187-195.
- 553 21. Díaz, D.d.O. and D.F. Hinz, *Performance of eddy-viscosity turbulence models for predicting*  
554 *swirling pipe-flow: Simulations and laser-Doppler velocimetry*. arXiv preprint  
555 arXiv:1507.04648, 2015.
- 556 22. Gandhir, A. and Y. Hassan, *RANS modeling for flow in nuclear fuel bundle in pressurized*  
557 *water reactors (PWR)*. Nuclear Engineering and Design, 2011. **241**(11): p. 4404-4408.
- 558 23. Hosokawa, S., et al., *Measurements of turbulent flows in a 2 x 2 rod bundle*. Nuclear  
559 Engineering and Design, 2012. **249**: p. 2-13.
- 560 24. Xiong, J.B., et al., *Laser Doppler measurement and CFD validation in 3 x 3 bundle flow*.  
561 Nuclear Engineering and Design, 2014. **270**: p. 396-403.
- 562 25. Holloway, M.V., D.E. Beasley, and M.E. Conner. *Investigation of Swirling Flow in Rod*  
563 *Bundle Subchannels Using Computational Fluid Dynamics*. in *14th International Conference*  
564 *on Nuclear Engineering*. 2006. American Society of Mechanical Engineers.
- 565 26. Conner, M.E., E. Baglietto, and A.M. Elmahdi, *CFD methodology and validation for single-*  
566 *phase flow in PWR fuel assemblies*. Nuclear Engineering and Design, 2010. **240**(9): p. 2088-  
567 2095.
- 568 27. Cinosi, N., et al., *CFD simulation of turbulent flow in a rod bundle with spacer grids (MATIS-*  
569 *H) using STAR-CCM*. Nuclear Engineering and Design, 2014. **279**: p. 37-49.
- 570 28. Podila, K. and Y.F. Rao, *CFD modelling of turbulent flows through 5 x 5 fuel rod bundles*  
571 *with spacer-grids*. Annals of Nuclear Energy, 2016. **97**: p. 86-95.
- 572 29. Chen, G.L., et al., *Design of a CFD scheme using multiple RANS models for PWR*. Annals of  
573 Nuclear Energy, 2017. **102**: p. 349-358.
- 574 30. Chen, X., et al., *Validation of CFD analysis for rod bundle flow test with vaned spacer grids*.  
575 Annals of Nuclear Energy, 2017. **109**: p. 370-379.
- 576 31. Chen, D.Q., et al., *Thermal-hydraulic performance of a 5 x 5 rod bundle with spacer grid in a*  
577 *nuclear reactor*. Applied Thermal Engineering, 2016. **103**: p. 1416-1426.
- 578 32. Xiong, J.B., et al., *CFD simulation of swirling flow induced by twist vanes in a rod bundle*.  
579 Nuclear Engineering and Design, 2018. **338**: p. 52-62.
- 580 33. Koncar, B. and S. Kosmrlić, *Simulation of turbulent flow in MATIS-H rod bundle with split-*  
581 *type mixing vanes*. Nuclear Engineering and Design, 2018. **327**: p. 112-126.
- 582 34. Li, X.C. and Y. Gao, *Methods of simulating large-scale rod bundle and application to a 17 x*  
583 *17 fuel assembly with mixing vane spacer grid*. Nuclear Engineering and Design, 2014. **267**: p.  
584 10-22.
- 585 35. Chen, G.L., et al., *CFD simulation for the optimal design and utilization of experiment to*  
586 *research the flow process in PWR*. Annals of Nuclear Energy, 2016. **94**: p. 1-9.
- 587 36. Liu, C.C., Y.M. Ferng, and C.K. Shih, *CFD evaluation of turbulence models for flow*  
588 *simulation of the fuel rod bundle with a spacer assembly*. Applied Thermal Engineering, 2012.  
589 **40**: p. 389-396.
- 590 37. Tseng, Y.S., Y.M. Ferng, and C.H. Lin, *Investigating flow and heat transfer characteristics in*  
591 *a fuel bundle with split-vane pair grids by CFD methodology*. Annals of Nuclear Energy,  
592 2014. **64**: p. 93-99.
- 593 38. Liu, C.C. and Y.M. Ferng, *Numerically simulating the thermal-hydraulic characteristics*  
594 *within the fuel rod bundle using CFD methodology*. Nuclear Engineering and Design, 2010.  
595 **240**(10): p. 3078-3086.
- 596 39. Lifante, C., et al., *3 x 3 rod bundle investigations, CFD single-phase numerical simulations*.  
597 Nuclear Engineering and Design, 2014. **279**: p. 60-72.

- 598 40. Agbodemegbe, V.Y., et al., *An investigation of the effect of split-type mixing vane on extent of*  
599 *crossflow between subchannels through the fuel rod gaps*. *Annals of Nuclear Energy*, 2016.  
600 **88**: p. 174-185.
- 601 41. Ikeda, K., Y. Makino, and M. Hoshi, *Single-phase CFD applicability for estimating fluid hot-*  
602 *spot locations in a 5 x 5 fuel rod bundle*. *Nuclear Engineering and Design*, 2006. **236**(11): p.  
603 1149-1154.
- 604 42. Navarro, M.A. and A.A.C. Santos, *Evaluation of a numeric procedure for flow simulation of a*  
605 *5 x 5 PWR rod bundle with a mixing vane spacer*. *Progress in Nuclear Energy*, 2011. **53**(8): p.  
606 1190-1196.
- 607 43. Sohag, F.A., L. Mohanta, and F.B. Cheung, *CFD analyses of mixed and forced convection in*  
608 *a heated vertical rod bundle*. *Applied Thermal Engineering*, 2017. **117**: p. 85-93.
- 609 44. Mao, H., et al., *Modeling of spacer grid mixing effects through mixing vane crossflow model*  
610 *in subchannel analysis*. *Nuclear Engineering and Design*, 2017. **320**: p. 141-152.
- 611 45. Lee, J.R., J. Kim, and C.H. Song, *Synthesis of the turbulent mixing in a rod bundle with vaned*  
612 *spacer grids based on the OECD-KAERI CFD benchmark exercise*. *Nuclear Engineering and*  
613 *Design*, 2014. **279**: p. 3-18.
- 614 46. In, W.K., et al., *Numerical computation of heat transfer enhancement of a PWR rod bundle*  
615 *with mixing vane spacers*. *Nuclear Technology*, 2008. **161**(1): p. 69-79.
- 616 47. Miller, D.J., F.B. Cheung, and S.M. Bajorek, *On the development of a grid-enhanced single-*  
617 *phase convective heat transfer correlation*. *Nuclear Engineering and Design*, 2013. **264**: p. 56-  
618 60.
- 619 48. Menter, F.R., *2-Equation Eddy-Viscosity Turbulence Models for Engineering Applications*.  
620 *Aiaa Journal*, 1994. **32**(8): p. 1598-1605.
- 621 49. Wilcox, D.C., *Reassessment of the Scale-Determining Equation for Advanced Turbulence*  
622 *Models*. *Aiaa Journal*, 1988. **26**(11): p. 1299-1310.
- 623 50. Wallin, S. and A.V. Johansson, *An explicit algebraic Reynolds stress model for*  
624 *incompressible and compressible turbulent flows*. *Journal of Fluid Mechanics*, 2000. **403**: p.  
625 89-132.
- 626 51. Yakhot, V., et al., *Development of Turbulence Models for Shear Flows by a Double*  
627 *Expansion Technique*. *Physics of Fluids a-Fluid Dynamics*, 1992. **4**(7): p. 1510-1520.
- 628 52. Holloway, M.V., et al., *The effect of support grid features on local, single-phase heat transfer*  
629 *measurements in rod bundles*. *Journal of Heat Transfer-Transactions of the Asme*, 2004.  
630 **126**(1): p. 43-53.
- 631 53. Acheson, D.J., *Elementary Fluid Dynamics*. 1990, New York: Oxford University Press.
- 632 54. Oberlack, M. and H.F. Busse, *Theories of Turbulence*. 2002, New York: Springer-Verlag  
633 Wien.
- 634 55. Tennekes, H. and J.L. Lumley, *A first course in Turbulence*. 1972, England The MIT Press
- 635